Quantifying sediment mass redistribution from joint time-lapse gravimetry and photogrammetry surveys

Maxime Mouyen[1], Philippe Steer[2], Kuo-Jen Chang[3], Nicolas Le Moigne[4], Cheinway Hwang[5], Wen-Chi Hsieh[6], Louise Jeandet[2], Laurent Longuevergne[2], Ching-Chung Cheng[5], Jean-Paul Boy[7], Frédéric Masson[7].

[1]Department of Earth and Space Sciences, Chalmers University of Technology, Onsala Space Observatory, SE-439 92 Onsala, Sweden.
[2]Univ Rennes, CNRS, Géosciences Rennes, UMR 6118, 35000 Rennes, France.
[3]Department of Civil Engineering, National Taipei University of Technology, Taipei 10608, Taiwan, R.O.C.
[4]Géosciences Montpellier, UMR CNRS/UM2 5243, Université Montpellier 2, CNRS, Montpellier, France
[5]Department of Civil Engineering, National Chiao Tung University, Hsinchu 300, Taiwan, R.O.C.
[6]Industrial Technology Research Institute, Hsinchu 310, Taiwan, R.O.C.
[7]Institut de Physique du Globe de Strasbourg, CNRS - Université de Strasbourg UMR 7516 - Ecole et Observatoire des Sciences de la Terre, 67084 Strasbourg Cedex, France.

Correspondence to: Maxime Mouyen (maxime.mouyen@chalmers.se)

Abstract. The accurate quantification of sediment mass redistribution is central to the study of surface processes, yet it remains a challenging task. Here we test a new combination of terrestrial gravity and drone photogrammetry methods to quantify sediment redistribution over a 1-km^2 area. Gravity and photogrammetry are complementary methods. Indeed, gravity changes are sensitive to mass changes and to their location. Thus, by using photogrammetry data to constrain this location, the sediment mass can be properly estimated from the gravity data. We carried out 3 joint gravity-photogrammetry surveys, once a year in 2015, 2016 and 2017 over a 1-km^2 area in southern Taiwan featuring both a wide meander of the Laonong River and a slow landslide. We first removed the gravity changes from non-sediment effects, such as tides, groundwater, surface displacements and air pressure variations. Then, we inverted the density of the sediment, with an attempt to distinguish the density of the landslide from the density of the river sediments. We eventually estimate an average loss of $4.7 \pm 0.4 \times 10^9$ kg of sediment from 2015 to 2017, mostly due to the slow landslide. Although the gravity devices used in this study are expensive and need week-long surveys, new instrumentation progresses shall enable dense and continuous measurements at lower cost, making this method relevant to improve the estimation of erosion, sediment transfer and deposition in landscapes.

1 Introduction

The reliable quantification of sediment mass redistribution is critical to the understanding of surface processes (Dadson et al., 2003; Hovius et al., 2011; Morera et al., 2017) and has significant implications for studies in tectonics (Molnar et al., 2007; Steer et al., 2014; Willett, 1999), climate (Peizhen et al., 2001; Steer et al., 2012), human activities (Horton et al.,

2017; Torres et al., 2017) or biochemistry (Darby et al., 2016). The earth's topography is constantly eroded but the rates of this erosion vary whether they are estimated at decadal, thousand- or million-years timescales. Estimating such erosion rates

35   over all these timescales provides a more complete description of their controlling processes (Dadson et al., 2003). These processes can run over millions to thousands years, such as tectonic uplift, in which case fission track thermochronometry (Fuller et al., 2006), cosmogenic nuclides (von Blanckenburg, 2006) or river terrace incision measurements (Hartshorn et al., 2002) are appropriate methods for estimating erosion rates. Nevertheless, rapid events such as earthquakes and landslides, very common in Taiwan, also play a significant role in eroding landscapes (Dadson et al., 2003; Hovius et al., 2000, 2011).

40   At daily to decadal timescales, erosion is classically estimated from the concentration of the suspended sediment in the rivers draining the studied areas (Fuller et al., 2003; Milliman and Farnsworth, 2011; Walling and Fang, 2003). A significant proportion of sediment can also be transported on the river bed (Blizard and Wohl, 1998), that is bedload sediment transport, which automatic gauging stations do not measure, likely resulting in an underestimation of the erosion rate. Nevertheless, sediment inputs to rivers in areas prone to landslides are not immediately flushed to the ocean. They are rather evacuated

45   over decadal timescales (Croissant et al., 2017; Hovius et al., 2011), generating large sediment redistributions, mixing suspended and bedload sediment transport, all along the rivers. Thus, this sediment redistribution should be quantifiable even with discontinuous observations. Here we develop a new approach, combining photogrammetry and terrestrial time-lapse gravimetry, to quantify such a sediment mass redistribution, over an area of ~1 km^2, in southern Taiwan. It aims at complementing suspended sediment measurements to better assess sediment redistribution at decadal timescales. The studied

50   area hosts both a slow landslide and a river carrying sediments eroded from the inner part of the mountainous catchment. The surveys were done once a year in 2015, 2016 and 2017.

Time-lapse gravimetry, that is the measure of gravity changes with time at a fixed location, is the only geophysical tool directly sensitive to mass redistributions at and below the earth's surface. It has been widely applied in the fields of glaciology, hydrology and solid earth processes, either from space, with the Gravity Recovery and Climate Experiment

55   (GRACE) mission (Farinotti et al., 2015; Han et al., 2006; Longuevergne et al., 2013; Pail et al., 2015; Tapley et al., 2004), or from terrestrial instruments (Van Camp et al., 2017; Crossley et al., 2013). Recent studies demonstrate the new potential of time-lapse gravity for studying surface processes as well, because the mass of deposited or eroded sediment can also significantly alter the gravity field (Liu et al., 2016; Mouyen et al., 2013, 2018).

The classical limitation for this method is the non-uniqueness of its solutions, since gravity changes are integrative and

60   sensitive to both mass variations and to the location where these mass variations take place (Fig. 1 and equation 1). Nevertheless, network gravity surveys have showed their high value to estimate below ground mass changes in hydrology (Jacob et al., 2010; Naujoks et al., 2008), volcanology (Carbone and Greco, 2007; Kazama et al., 2015) or reservoir monitoring evolution (Ferguson et al., 2008; Hare et al., 2008). Unlike deep mass changes, sediment redistributions occur at the ground's surface and are therefore accessible to accurate location methods such as photogrammetry (Eltner et al., 2016;

65   Niethammer et al., 2012; Schwab et al., 2008). Combining accurate geometries with gravity variations must thus enable

proper mass estimations. Fig. 1 illustrates the use of time-variable gravimetry to quantify sediment mass redistribution at the earth's surface. The change of gravity Δg measured between t_0 and t_1 is:

$$\Delta g = g_{t1} - g_{t0} = \sum_{i=1}^{N} \Delta g_i = \sum_{i=1}^{N} \frac{Gm_i}{r_i^2} \sin \theta \tag{1}$$

where Δg_i is the vertical component of the gravitational change at each element i (i ranging from 1 to N = 28 in Fig. 1b)

70   considered as a point-mass (Fig. 1c) of mass m_i located at a distance r_i from the gravimeter, and G is the universal gravitational constant. Note that the gravitational attraction of any element decreases with the square of the distance between this element and the site where gravity is measured, so that the distance of the mass redistribution can be a strong limiting factor to measure significant gravity changes.

Testing the combination of photogrammetry and gravimetry for monitoring surface processes is a valuable effort regarding

75   the recent and ongoing progress in gravimetry (Ménoret et al., 2018; Middlemiss et al., 2016, 2017), which shall open new ranges of applications and trigger interests outside the field of geodesy.

After introducing the study area, we describe the gravimetry and photogrammetry surveys that we conducted, together with our data processing workflow. We then show the results of both methods and interpret them jointly in order to retrieve the mass of sediment redistributed in this area from 2015 to 2017. We eventually discuss the benefits and limits of this method.

80   **2 Study area**

The joined gravimetry-photogrammetry survey was set in southern Taiwan, at the Paolai village, next to the Laonong River (Fig. 2). The gravity network contains one site, AG06, for absolute gravity (AG) measurement and nine sites, BA01 to BA09, for relative gravity (RG) measurements. During the 2017 survey, all sites but BA02 were located to cm accuracy using Global Navigation Satellite System (GNSS) enhanced by real-time kinematic (RTK) technique. The location of BA02

85   could not be measured due to the unexpected storage of concrete blocks, referred to as dolosse, aiming at being placed on the river shore to protect it from erosion. This dolosse storage also covered BA03 and BA04, although those two sites could be reached since these blocks are not plain. Their gravimetric effect will be estimated and removed from the measurements.

The first reason for choosing this location is that time-lapse absolute gravity surveys have been done at AG06 since 2006, in the frame of the Absolute Gravity in the Taiwan Orogen (AGTO) project. This project permitted to identify, for the first

90   time, sediment redistribution using time-lapse absolute gravimetry and shown that significant sediment transfers occurred around Paolai (Kao et al., 2017; Mouyen et al., 2013). Indeed, this site experiences vigorous sediment transfer processes powered by heavy rains brought by tropical cyclones (typhoons) and monsoonal events, especially in May to August (Chen and Chen, 2003). The heavy rains destabilize the slopes of the Taiwanese high mountains, triggering landslides and debris flows (Chiang and Chang, 2011). This occurs on a regular basis: 5 to 6 typhoons make landfall in Taiwan every year (Tu et

95   al., 2009), mostly between May and September. The most remarkable event was the 2009 Morakot typhoon, which produced the worst flooding in the last 60 years in Taiwan and up to 2777 mm of accumulated rainfall (Ge et al., 2010) and triggered

22 705 landslides with a total area of 274 km^2 (Lin et al., 2011). Landsliding, which can also be triggered by regional active tectonics, is the main process supplying sediment to rivers in Taiwan (Dadson et al., 2003; Hovius et al., 2000).

The second reason for choosing this location is practical. Indeed, this location offers a stabilized path made of concrete on
100   the southern bank of the Laonong River, where the relative gravity benchmarks could be properly set, on stable and sustainable sites, and easily accessed for measurements. Also, a continuous GNSS station, PAOL (latitude: 23.10862°, longitude: 120.70287°, elevation: 431 m), is co-located with the AG06 pillar and is maintained by the Institute of Earth Sciences-Academia Sinica (IES-AS, 2015). This permits to precisely take into account gravity changes only due to ground vertical displacements.

105   In this area, both the Laonong River and the landslide (Fig. 2) are susceptible to sediment transfers. The gravimetry-photogrammetry survey is setup to focus on these processes. Note that what we call the river (plain black line contour in Fig. 2) is the active channel bed that includes emerged alluviums. During yearly measurements, the water extent of the river only covers a fraction of this area, even if the period 2015-2017 has seen some higher water level and larger extents, especially during large floods.

110   **3 Methods**

3.1 Time variable gravimetry

Gravity was measured at 10 sites (Fig. 2) in November 2015, 2016 and 2017, as the climatic conditions are usually suitable for gravimetry fieldwork during this month (e.g. no typhoon nor heavy rains, reasonable temperatures). By measuring gravity during the same period of the year, we also expect to minimize hydrological effects, which have an strong annual
115   periodicity in this area (Chen and Chen, 2003).

Relative gravity measurements were done using a Scintrex CG5 Autograv (serial number 167). The measurement principle is to assess length variations of a spring holding a proof mass between different times and places, using a capacitive displacement transducer, and convert them into gravity variations (Scintrex Ltd., 2010). The instrument is leveled at each site and repeats 90-seconds measurements continuously. We stop measurements when gravity readings repeat within 3 μGal
120   (1 μGal = 10^{-8} m s^{-2}), while the internal sensor temperature remains stable. This usually takes 10 to 15 measurements, that is 15 to 23 minutes, although up to 25 measurements were required in some rare cases. Relative gravimeter measurements are subjected to an instrumental drift, which is corrected using the software Gravnet (Hwang et al., 2002). Inferring this drift requires to regularly re-measure a base station where absolute gravity is known (AG06 in this case) and at least to start and finish the survey at this base station. In addition, ambient temperature alters gravity measurements at a rate of -0.5 Gal °C^{-1}
125   (Fores et al., 2017). This effect was taken into account before adjusting the instrumental drift of the gravimeter.

The absolute gravity measurements were done using a Micro-g FG5 (serial number 224), which monitors the drop of a free-falling corner-cube in a vacuum. During its free fall, the positions and times of the corner-cube are precisely assessed using laser interferometry and an atomic clock (Niebauer, 2015; Niebauer et al., 1995). One measurement takes ~12 hours and

consists in 24 sets of 100 test mass drops started every 30 min (one drop every 10 s). Measurements are always done
130 overnight, when anthropogenic seismic noise and temperature variations are lower than during day time. A laser problem in
the FG5 prevented us from measuring absolute gravity in 2017. This is compromising since the measurements at BA01-
BA09 can only be interpreted relative to an absolute reference. A first option would be to disregard the gravity data
measured in 2017 and not interpret the relative gravity changes between 2016 and 2017. This is a rather drastic solution and
we prefer to use a likely gravity value for AG06 in 2017, keeping in mind that we may thus introduce an unknown but
135 constant offset in the whole relative gravity data. The absolute gravity value at AG06 was measured in 2014, 2015 and 2016
(Fig. 3) and we extrapolate the 2017 value as being the average of the three previous AG values, that is
978 713 845.1 ± 3 µGal. We arbitrarily set the standard deviation to a value larger than usual at this site. In this case, the
AG06 values in 2016 and 2017 are quite similar, less than 0.5 µGal difference.

To focus on sediment redistribution, other sources responsible for gravity changes must be removed from the gravity time
140 series. Here, these effects are the tides, air pressure variations, polar motions, vertical ground motions and hydrology. These
corrections are detailed in the next paragraph and summarized in Table 1.

Solid earth tides are computed using TSOFT (Van Camp and Vauterin, 2005) using tidal parameters from Dehant *et al.*
(1999), referred to as WDD. Ocean tide loading effects are computed using the FES2004 model (Letellier et al., 2004) with
the Ocean Tide Loading provider (Bos and Scherneck, 2003). Polar motions effects are computed using the International
145 Earth Rotation and Reference System Services parameters and the Absolute Observations Data Processing Standards
(Boedecker, 1991). Atmospheric effects, that is gravity changes due to air masses, are corrected using local barometric
records done at a continuous weather station located ~12 km west of Paolai (station name C0V250) and an admittance factor
of -0.3 µGal hPa^{-1} (Merriam, 1992). Vertical displacements of the ground also change the gravity, because the gravity
measured at any place on the Earth's surface depends on the inverse of the square of the distance between this site and the
150 Earth's center of mass. Therefore, if the site is uplifting (further from center of mass) or subsiding (closer to the center of
mass), it will have a lower or higher gravity value, respectively. This effect is corrected using continuous GNSS time series
recorded at AG06 (site PAOL, Fig. 4) and assuming a theoretical ratio $\varDelta g/\varDelta z$ = -2 µGal/cm (Van Camp et al., 2011), where
$\varDelta g$ is the gravity change and $\varDelta z$ is the elevation change, at the same location.

We also correct the effect of hydrology, which deforms the earth surface at the global scale and changes the groundwater
155 mass attraction at local scales, near the gravimeter. This correction relies on global hydrological models. We consider two of
them in this study:

1. the Global Land Data Assimilation System Version 2 (GLDAS-2) forcing the Noah land surface model (Rodell et
    al., 2004) and
2. the Modern-Era Retrospective Analysis for Research and Applications, version 2 (MERRA-2, Gelaro et al., 2017).

160 The gravitational effect due to each of these models is provided by the EOST loading service (Boy, 2015; Petrov and Boy,
2004). Unlike the other corrections, the hydrological correction may suffer large uncertainties because of (1) the complexity

of hydrological processes, (2) the difficulty to measure groundwater and (3) its large effect on gravity (Jacob et al., 2009; Longuevergne et al., 2009; Pfeffer et al., 2013). Indeed, the effect of GLDAS-2 and MERRA-2 on gravity predict up to 20 µGal of seasonal amplitude in the hydrological signal, with sometimes large differences, up to 10 µGal, between the
165 different models (Fig. 5).

Nevertheless, surveying in November appears as a valuable way to decrease the hydrological impact on the gravity data, since this effect is lower than 3 µGal, with any of the two hydrological models. Eventually we use the average hydrological effect from GLADS-2 and MERRA-2. We arbitrarily set an uncertainty of 5 µGal to this correction (Table 1), to account for possible bias in the models.

170 Note that we also correct the effect of the dolosse set in 2017, which is only significant at BA03 and BA04. These structures, located above BA03 and BA04, were indeed responsible for an artificial decrease of gravity of about 15 µGal (computation details in Appendix A). Given the uncertainty of this correction process, we add an arbitrary 5 µGal uncertainty on the gravity changes measured at BA03 and BA04 during the 2017 survey.

3.2 Photogrammetry

175 An Unmanned Aerial Vehicle (UAV), commonly known as a drone, is an aircraft without human pilot on board and has been used in many disciplines, especially in morphotectonic studies (Chang et al., 2018; Deffontaines et al., 2017, 2018). To generate a high-resolution digital surface model (DSM), orthorectified mosaic images, and a true 3D model, the UAV mounted with a Sony ILCE-QX1 camera and a 16 mm SEL16F2.8 lens was used in this study (Fig. 6). The UAV is a modified already-available Skywalker X8 fixed-wing aircraft reinforced by carbon fiber rods and Kevlar fiber sheets.
180 Launched by hand, it flies, takes photos, and lands autonomously by using a pre-programmed flight plan. The autopilot system is composed and modified from the open source APM (Ardupilot Mega 2.6 autopilot) firmware and open source software Mission Planner, transmitted by ground-air XBee radio telemetry.

The flight missions were planned with 300-500 m mean above ground level, covered an area of about 15-20 km^2 with about 10-15 cm ground sampling distance (GSD) in one single flight mission. Repeated adjacent photographs were kept for at least
185 85 % endlap and 50 % sidelap. Each UAV flight missions took about 90 min. The data sets, including orthomosaic images, DSM, and true 3D model, were generated and processed using ContextCapture and Pix4Dmapper with a grid spacing of 50 cm. 21 ground control points and 11 check points were measured in the field to control and to verify the quality of the datasets (Fig. 6c).

4 Survey results

190 The results of the gravity and photogrammetric surveys are shown in Figs. 7 and 8, respectively. The largest gravity changes occurred between 2015 and 2016, with most sites showing an increase of more than 30 µGal. On the contrary, the gravity decreased at most sites from 2016 to 2017. When measured above the redistributed masses, increase and decrease of gravity

correspond to gain and loss of masses, respectively. Qualitatively, this is in agreement with the corresponding digital surface models (DSM) changes in the active bed channel showing higher sediment thicknesses, thus a gain of mass, from 2015 to

195 2016 and large surfaces of lower sediment thicknesses from 2016 to 2017. Over the time period 2015-2016, the top of the landslide is actively eroded, up to 46 m, while its toe displays significant sedimentation, up to 33 m. The active river bed shows a mixed-pattern of erosion and sedimentation, between -1.19 and 1.21 m on average, possibly resulting from the migration of the river braids. Whereas, over the time period 2016-2017, the landslide displays mostly erosion, up to 39 m, while the river bed continues to display a mixed-pattern of erosion and sedimentation, between -1.17 and 1.08 m on average.

200 The gravimetric and photogrammetric techniques show large changes in gravity and topography, which demonstrate active processes of sediment redistribution in the river and on the slow landslide. In the next section, we combine these results to assess the mass of sediment redistributed from 2015 to 2017. Note that we focus the DSM analysis to the area bounded by the black line in Figs. 8d and 8e, which is restricted to the landsliding zone and the river.

5 Joint analyses of the gravity and photogrammetry data

205 Using the DSM, we build rectangular prisms with horizontal sides of 0.5 m, i.e. DSM resolution, and a vertical side as high as the elevation at the time of the corresponding surveys, i.e. bottom at 0 m and top at the surface elevation. Among the three (2015, 2016 and 2107) photogrammetric surveys, the 2017 survey has the smallest surface extent. Its limits are thus used to cut the 2015 and 2016 photogrammetric surveyed areas, so that all DSM cover the exact same area. The total mass of redistributed sediment equals the change of volume between each survey multiplied by the density of the sediment. We use

210 the gravity data to assess this density using an inverse modelling approach. Note that since gravity decreases with the square of the distance between the measurement site and the mass location, we can bound our analysis to the area covered by the photogrammetric surveys without biasing the analysis. Indeed, using the wider 2015 and 2016 survey coverages, we find that extending our working area in the north-south and east-west directions by steps of 100 m does not alter the gravity changes computed at each sites by more than 1 %.

215 We design three inversion cases to retrieve the densities of the redistributed materials, using a least-square criterion. These cases are independent from each other and aim at increasing the amount of possibly different densities for comparison. Thus we invert:

- Case 1: The average density ρ of the material redistributed during the surveys.
- Case 2: The density of the sediment in the river ρ_r and the density ρ_l of the material in the landslide.
220 - Case 3: The density of the sediment in the river ρ_r^{1615} from 2015 to 2016 and ρ_r^{1716} from 2016 to 2017 and the density ρ_l of the material in the landslide.

Here we will solve an over-determined problem, where we have more observations (20 gravity differences over the three years) than variables to estimate (density, three at most, in case 3). However, gravity observations are too few and unevenly

distributed over the study area to try to invert the density at each pixel (more than 4 millions) of the photogrammetry survey.

225 In practice, the matrix representation of this system is (e.g. Hwang et al., 2002)

$$\mathbf{L} + \mathbf{V} = \mathbf{AX} \tag{2}$$

where the design matrix $\mathbf{A}$, vector of unknowns $\mathbf{X}$ and vector of observations $\mathbf{L}$ are defined as

$$\mathbf{A} = \begin{bmatrix} dg_{mod,r}^{1615,BA01} & 0 & dg_{mod,l}^{1615,BA01} \\ \vdots & \vdots & \vdots \\ dg_{mod,r}^{1615,PAOL} & 0 & dg_{mod,l}^{1615,PAOL} \\ 0 & dg_{mod,r}^{1716,BA01} & dg_{mod,l}^{1716,BA01} \\ \vdots & \vdots & \vdots \\ 0 & dg_{mod,r}^{1716,PAOL} & dg_{mod,l}^{1716,PAOL} \end{bmatrix} \tag{3}$$

$$\mathbf{X} = \begin{bmatrix} \rho_r^{1615} \\ \rho_r^{1716} \\ \rho_l \end{bmatrix} \tag{4}$$

$$\mathbf{L} = \begin{bmatrix} dg_{obs}^{1615,BA01} \\ \vdots \\ dg_{obs}^{1615,PAOL} \\ dg_{obs}^{1716,BA01} \\ \vdots \\ dg_{obs}^{1716,PAOL} \end{bmatrix} \tag{5}$$

and $\mathbf{V}$ is the vector of residuals ($\mathbf{X}$ and $\mathbf{V}$ are to be determined by the least-squares method). In matrices $\mathbf{A}$ and $\mathbf{L}$, dg is the gravity variation that is modelled (dg_{mod}) or observed (dg_{obs}) between 2016 and 2015 (1615) or between 2017 and 2016 (1716) at every site (BA01… PAOL). The modelled gravity change can be computed for the material in river ($dg_{mod,r}$) or in the landsliding zone ($dg_{mod,l}$). This matrix representation is given for the inversion case 3 and can be simplified for cases 1

235 and 2.

The design matrix $\mathbf{A}$ is built thanks to the photogrammetry surveys, from which we identify the river and the landslides as well as their respective volume changes. Therefore, knowing also the position of the gravity sites, we compute each element of $\mathbf{A}$ using a 3D gravity modelling by prisms methods (Nagy, 1966) and an arbitrary density equal to 1. The actual density can be inverted by

240 $$\mathbf{X} = (\mathbf{A}^T \mathbf{P} \mathbf{A})^{-1} (\mathbf{A}^T \mathbf{P} \mathbf{L}) \tag{6}$$

where $\mathbf{A}^T$ is the transpose of $\mathbf{A}$. The weight matrix $\mathbf{P}$ is diagonal, and its elements are the invert of the gravity uncertainties at each site i. Finally, the residuals $\mathbf{V} = \mathbf{AX} - \mathbf{L}$ are used to compute the uncertainty of the inverted densities as

$$\sigma_d = \mathbf{V}^T \mathbf{P} \mathbf{V} / (n - u) \tag{7}$$

where n is the number of gravity observations and u the number of unknown densities. The inverted densities for each case

245 are summarized in Table 2. Cases 1 and 2 returns similar densities. Case 3 returns a noticeable difference between the densities of the sediment in the active bed channel for the 2015/2016 or 2016/2017 surveys. A first hypothesis for this difference could be that the composition of the redistributed sediment has changed over the years of the study, for instance

because they come from landslides that occurred in terrain with different densities. A second hypothesis is that the water content of the sediment varies, eventually changing the effective density of the sediment as measured by the gravimeters. We do not have enough data to favor one of these hypothesis but we will discuss the possible influence of water on our density estimates in section 6.1. Uncertainties on the landsliding materials densities (case 2 and 3) are higher than those of the river sediment, likely because they are further from the gravity sites than the river sediment. As seen in equation 1, the further the redistributed masses are, the lower are their gravitational effects.

For comparison, during the 2017's survey, we evaluate the in situ densities of the materials in the active river bed and at the bottom of the landslide, at 22 sites (Fig. 9), also using photogrammetry (Appendix B). The in situ densities range from 1.2 to 2.7×10^3 kg m^{-3} and are spatially heterogeneous, illustrating the variety of materials carried by the river and the landslide. Despite the limited and spatially uneven sampling points, we obtain an average density (2.0×10^3 kg m^{-3}) consistent with the average densities inverted from the gravity and photogrammetry data (1.9×10^3 kg m^{-3}).

The final comparison of the measured gravity and the computed gravity in cases 1, 2 and 3 is given in Fig. 10. The largest misfits are at BA05 and BA06 during the 2017-2016 period, for which gravity changes are underestimated by 19 and 15 μGal, respectively. Possible explanations for these two misfits are: a wrong site location, an error in the gravity data or an error in the DSM data, yet we could not narrow our search down a specific issue at BA05 and BA06. At the other sites, the pattern and amplitude of the gravity observations is rather well explained by the modelling, showing the interest of coupling gravity and photogrammetric surveys to retrieve the density of the redistributed materials. Note that in Fig. 10b, the gravity modelled at most sites seems to need a small offset of -3 μGals to fit within the error bars of the observations. This may show that our absolute gravity estimate for the 2017 survey (Fig. 3) is wrong by 3 μGals.

Multiplying the inverted densities (Table 2) with the volumes changes computed from the DSM changes, we can eventually compute the mass of sediment that were redistributed between two surveys, for each inversion cases (Fig. 11). Since the inverted densities are similar in each three case (Table 2) and the volumes changes estimated from photogrammetry are identical, thus the estimated masses (volumes times density) are also similar in each three case. The difference mostly lies within the uncertainty of these estimates. In our mass estimation, we also differentiate the top and the toe of the landslide, because the top of the landslide mostly experience erosion, while its toe undergoes both erosion and sedimentation processes. This helps to unravel how the sedimentation and erosion processes are distributed over the slow landslide.

In the river only, we observe that the mass of sediment redistributed between each survey is similar. The river gained between 0.61 and 0.83×10^9 kg and lost between 0.58 and 0.74×10^9 kg. Thus, the mass loss is about 4% and 12% less than the mass gain, resulting in a quasi-balanced budget that is within the uncertainty of the mass estimations. The time variability of the sediment mass budget is dominated by the landslide, which causes larger mass redistributions (up to 4×10^9 kg) and loss-to-gain ratios. A significant mass loss occurred between 2016 and 2017, which is ~15 times larger than the mass gain. Between 2015 and 2016, both erosion and sedimentation are significant at about 2 to 3×10^9 kg, which are rather balanced. A likely hypothesis is that we mainly observe a transfer of sediment from the top of the landslide, where $2.1 \pm 0.6 \times 10^9$ kg of material were eroded toward its toe to accumulate $1.9 \pm 0.5 \times 10^9$ kg here (average mass from the three cases). Overall, from

2015 to 2017, the area has lost about $4.7 \pm 0.4 \times 10^9$ kg of sediment. Note that this landslide occurs over several years, not in one quick event, probably as the consequence of the erosion by the meandering Laonong River.

6 Discussion

6.1 Implications for sediment transfers in active landscapes

Our results highlight how landscapes react to landsliding and how they evolve after a large perturbation such as the 2009 Morakot typhoon. Between 2015 and 2016, the activity of the Paolai slow landslide mostly consists in transferring about 2×10^9 kg (about 1×10^6 m^3) of materials form the landslide top to the landslide toe over roughly 100 to 200 m. After 2016, a significant event of erosion of the landslide occurs, with more than 3×10^9 kg of sediment removed, including most of the sediment previously deposited on the landslide toe. This corresponds to a particularly rapid evacuation of the sediment, especially in the alluvial context of the Laonong river, that is yet consistent with predictions obtained with a morphodynamic model by Croissant et al. (2017) for bedrock rivers. It is likely that the position of the landslide in the outer bank of a meander has favored sediment export efficiency. Despite this landslide activity, it is quite remarkable that the Laonong river roughly maintains a neutral sediment budget over 2 years, between 2015 and 2017, in the vicinity of the landslide. This means that the river mainly acts as a sediment transfer zone and that river incision and sediment evacuation occurring along the river is balanced by the sediment delivery occurring by the supply of landslide materials. This sediment supply may originate from the several large landslides triggered in the Paolai area by the 2009 Morakot typhoon (Lin et al., 2011) and the following massive sediment aggradation along fluvial valleys up to 10, 30 and even possibly 100 m (DeLisle and Yanites, 2018; Hsieh and Capart, 2013). Our results would thus suggest that the Laonong river has not yet recovered from this aggradation phase and that the landscape is still perturbed by the aftermath of Morakot typhoon, even 8 years after its occurrence. This exceeds the relaxation time of 6 years observed after the 1999 Chi-Chi earthquake using river suspended load (Hovius et al., 2011). But typhoon-triggered landslides occur every year in Taiwan, and global warming may intensify this process (Chiang and Chang, 2011). This could also build and maintain long-term sediment sources within the Taiwan range, which will keep supplying sediment into rivers even long after the Morakot-induced sources have been completely flushed.

6.2 Impact of river water storage changes

The mass of sediment redistributed in the studied area from 2015 to 2017 was computed by multiplying the volume of redistributed sediment by a density estimated from the joint analysis of gravity and photogrammetry data. We tested several ways of separating materials: active river bed or landslide materials and active river bed material between 2015 and 2016 or between 2016 and 2017. However, the active river bed also includes the actual Laonong River, that is water with density $\rho_w = 10^3$ kg m^{-3}. The photogrammetry actually measures the river surface but we did not make the distinction between the water and the active river bed because the bathymetry of the river is unknown. Consequently, without the river depth's

geometry, we cannot turn the river into 3D prisms for computing its gravity effect. As a workaround, here we simply assume

a constant river depth of 1 m, that corresponds to very rough field estimates. Then, we map the surface limits of the river

315 from the optical images taken by the UAV during each survey. The height h of the river surface is given by the

photogrammetry results. The river is then divided into prisms covering the river area, with sides of 0.5 m, upper face at

elevation h and lower face at elevation h-1, since the river is 1-m deep. We then compute the gravity effect of the river on

each site of the network (except BA02, which position is unknown). Eventually, this effect is removed from the gravity

observation and the average density inversion (case 1) is run, giving $\rho = 1.7 \pm 0.1 \times 10^3$ kg m^{-3} and RMS = 9.7 µGal. This

320 represents a decrease of 11% relative to the density $\rho = 1.9 \pm 0.2 \times 10^3$ kg m^{-3} given in Table 1 and also relative to the

mass budget in Fig. 11. These values are yet to be taken with caution since we do not know the exact geometry of the river,

its depth in particular.

6.3 Perspectives from recent progresses in gravimetry

In this study we take advantage of the intense surface processes occurring in Taiwan to jointly analyze both time-variable

325 gravity and photogrammetry measurements. Indeed, the amplitude of the sediment redistribution guarantees to measure

significant gravity changes and, most importantly, surface elevation changes. Nevertheless, for rivers experiencing large and

dynamic sediment redistributions that yet remain hidden beneath the water level, photogrammetric data would not bring any

constraint on the density inversion. One should thus only rely on the gravity measurements, leading to non-uniqueness

problem, since both the density and the location of the redistributed sediment would have to be inverted. To better deal with

330 this issue, we suggest two improvements to our gravity survey:

1. Set a denser network of gravity sites, ideally with a mesh structure. Indeed, more measurements, evenly distributed,
   means more constraints on the density-location inversion.

2. Set this network closer to the mass changes to increase the gravity signal. The best option would be to locate the
   gravimeters directly beneath the river bottom. Fig. 12 shows that for such gravimeters, the average gravity change
335 would increase from 31 to 50 µGal between 2016 and 2015 and from 13 to 61 µGal between 2017 and 2016.

This survey implies that gravimeters are set permanently over the time-period of the project, as they won't be easily

accessible. Such a setup of buried permanent gravimeters is presently impossible to realize with CG5 or any other

contemporary relative or absolute gravimeter, but remains realistic at a few-years timescale. Indeed, a new generation of

relative gravimeters is rising from the use micro-electro-mechanical systems (MEMS) technology, characterized by a

340 significantly smaller size and lower price (Liu and Pike, 2016; Middlemiss et al., 2016, 2017). Those shoebox-sized

devices could be used to set permanent and dense gravity networks in areas experiencing vigorous sediment transport.

Gravity changes densely sampled over the river will permit to retrieve the sediment redistribution (both mass change

and position) using gravity inversion methods (e.g. Camacho et al., 2011) further constrained by the geometry of the

river and the depth of the relative gravimeter. In addition, as relative gravimeters suffer from instrumental drift, this

345   buried permanent network should be run in parallel to either permanent absolute measurements, which has recently
       become possible thanks to quantum gravimeters achieving 1 µGal repeatability (Ménoret et al., 2018), or to slowly
       drifting superconducting gravimeters (Hinderer et al., 2015). Therefore, ongoing progresses in the development of
       terrestrial gravimeters may open new opportunities for quantifying the mass of sediment redistributed by surface
       processes. Another interest for having such a permanent gravity network is to monitor the dynamics of the sediment
350   redistribution at timescales shorter than one year, since the sediment concentration in Laonong river varies across the
       year (Fig. 13a).

6.4 Continuous sediment transport estimation

When sediment concentration is not continuously measured, sediment rating curves are a convenient workaround which
permits, once determined, to estimate sediment transport from water discharge measurements only (Horowitz, 2003). Indeed,
355   continuous water discharge is less complicated to measure than sediment concentration. But this method, which does not
properly capture the bedload transported sediment, is inappropriate for landslide-dominated mountain belts such as Taiwan
(Blizard and Wohl, 1998; Hovius et al., 2000). In addition, sediment rating curves experience temporal variation (Huang and
Montgomery, 2013; Morera et al., 2017) and can also be altered by the release of groundwater (Andermann et al., 2012).
Thus, the proper use of rating curves is bounded to specific conditions that are yet to be validated for the Laonong River.
360   Here we discuss the use of gravity for measuring the total sediment discharge of the Laonong River, that is suspended and
bedload sediment transport.

The method and perspectives introduced so far aim at quantifying the mass of sediment redistributed by an event with large
sediment transport ability, such as a landslide or a high river discharge. Thus, the time step of this quantification depends on
how long these events take to redistribute the sediment in a way that significantly alter the gravity measured at each site by,
365   e.g., >10 µGal, as an indicative change. Fig. 13a shows that the largest sediment concentration recorded at LiuGui station is
5000 ppm (mass fraction), when the river level increased by 1.6 m.

For the hypothetical buried gravity network (Fig. 12c), we compute the gravity effect of a river level change of 1.6 m, which
covers the entire area of the active bed channel of Laonong River. The 5000-ppm sediment concentration means there is 5 kg
of sediment in 1000 kg of river's fluid, hence 995 kg of pure water. In this framework, and assuming that the density of the
370   sediment is 2×10^3 kg m^{-3}, we can compute the density change due to rising sediment concentrations, until 10^6 ppm, meaning
the river is made of sediment only. The gravity variation solely due to 5000 ppm of suspended sediment is about 0.17 µGal
on average over each site. This cannot be properly distinguished from the main gravity change due to the rising river water
level. Thus, time-variable gravity would not have been sensitive to the instantaneous suspended sediment concentration of
the Laonong River between 2015 and 2017, even with a gravity network beneath the riverbed. In fact, the suspended
375   sediment concentration should be about 3×10^5 ppm to change the gravity by at least 10 µGal (Fig. 13b with the bedload set to
0 cm). This corresponds to a strong debris-flow, nearly 8 times more concentrated than the threshold of 4×10^4 ppm used for
debris-flow definition (Dadson et al., 2005; Lin and Chen, 2013). However, sediment is also transported on the river bed, as

bedload, and it must be added to suspended sediment concentration to make a complete estimation of the sediment discharge effect on gravity. We have no measurement of this bedload component for Laonong River but measurements in another

380 catchment of Taiwan showed that 50% of the cumulative mass of the bedload was built by rocks which diameter is 15 cm (D_{50} = 150 mm) and D_{90} = 62.5 cm (Cook et al., 2013). Therefore, we compute the effect of homogenous bedload layers of up to 60 cm thickness and density 2×10^3 kg m^{-3} and add it to the suspended sediment effect (labelled curves in Fig. 13b). It generates about 50 µGal of gravity variation, which would be clearly identifiable in the gravity measurements. This computation gives an order of magnitude of the gravity change expected from time-varying suspended and bedload

385 transport. It shows that continuous time-variable gravity could quantify sediment discharge if the sediment concentration is at least 3×10^5 ppm without bedload, or if the bedload is at least 12.5 cm thick, under the assumption that only gravity changes above 10 µGal are significant. Again, this 10-µGal threshold is linked to the accuracy of todays' gravimeter but ongoing progresses and interest in time-variable gravimetry may fuel the development of devices with higher accuracies.

7 Conclusion

390 This study shows that the mass of sediment redistributed by rivers and landslides can be estimated by combining time-lapse gravimetric and photogrammetric measurements. Focusing on the Laonong River, in southern Taiwan, we estimate that about $4.7 \pm 0.42\times10^9$ kg of sediment were removed from 2015 to 2017 around our study site. This sediment loss is mainly due to a slow landslide moving from one year to another. The sediment budget (i.e. the difference between sedimentation and erosion) within the river is close to zero, although more surveys should be carried out to identify longer-term deposition

395 or erosion in this area. The average sediment density obtained with this method ($1.9 \pm 0.2\times10^3$ kg m^{-3}) is similar to the average sediment density measured in situ across the flood plain (2.0×10^3 kg m^{-3}). The new method introduced in this paper has the advantage to directly sense the mass of sediment, without using rating curves or in situ sediment concentration data. Therefore, it can benefit a wealth of studies on surface processes, which require quantitative estimates of sediment redistribution. Although time-variable gravimetry remains a rather expensive method with demanding survey constraints, it

400 has undergone promising progresses in the recent years. One is the significant miniaturization of the devices, using inexpensive MEMS technology (Middlemiss et al., 2016), the other is the realization of permanent absolute gravimeters, using cold-atom interferometry (Ménoret et al., 2018). Such new tools could be further used without photogrammetry, for rivers where most of the sediment transport is hidden under the water. If the suspended and bedload transport are significant enough, measuring the instantaneous sediment discharge could also become a reasonable project.

405 **Data availability**

Data are available from the corresponding author on reasonable request.

Author contribution

P.S., M.M. and L.L conceived the study. M.M., N.L.M. and W.-C.H. acquired and processed the gravimetry data. K.-J.C. acquired and processed the photogrammetry data. L.J. and M.M. made the in situ sediment density measurements. C.H.
410 acquired and processed the GPS-RTK data. J.-P.B. computed the hydrological loading effect on gravity. M.M. performed the main analysis. All authors contributed to the final form of the article.

Competing interests:

The authors declare that they have no conflict of interest.

Acknowledgments

415 M.M. did the fieldwork and part of the analysis study while being a postdoctoral researcher at Geosciences Rennes, supported by a postdoctoral grant of the Centre National d'Etudes Spatiales (CNES) and by the CRITEX project funded by the Agence Nationale de la Recherche (ANR-11-EQPX-0011 and the Brittany region). We acknowledge support by the EROQUAKE project funded by the Agence Nationale de la Recherche (ANR-14-CE33-0005) and from the France-Taiwan International Associate Laboratory "From Deep Earth to Extreme Events" (LIA-D3E, http://www.lia-adept.org/). We are
420 grateful to the RESIF-GMOB (http://www.resif.fr) facility for providing us with the relative gravimeter Scintrex CG5 #167. The authors acknowledge the Taiwan Typhoon and Flood Research Institute, National Applied Research Laboratories, for providing the Data Bank for Atmospheric & Hydrologic Research service.

References

Andermann, C., Bonnet, S., Crave, A., Davy, P., Longuevergne, L. and Gloaguen, R.: Sediment transfer and the hydrological
425 cycle of Himalayan rivers in Nepal, Comptes Rendus Geosci., 344(11), 627–635, doi:https://doi.org/10.1016/j.crte.2012.10.009, 2012.

von Blanckenburg, F.: The control mechanisms of erosion and weathering at basin scale from cosmogenic nuclides in river sediment, Earth Planet. Sci. Lett., 242(3), 224–239, doi:https://doi.org/10.1016/j.epsl.2005.11.017, 2006.

Blizard, C. R. and Wohl, E. E.: Relationships between hydraulic variables and bedload transport in a subalpine channel,
430 Colorado Rocky Mountains, U.S.A., Geomorphology, 22(3), 359–371, doi:https://doi.org/10.1016/S0169-555X(97)00055-X, 1998.

Boedecker, G.: IAGBN: Absolute Observations Data Processing Standards, BGI-Bull. d'Information, 69, 25, 1991.

Bos, M. S. and Scherneck, H.-G.: Ocean tide loading provider, [online] Available from: http://holt.oso.chalmers.se/loading/, 2003.

435   Boy, J.-P.: EOST Loading Service, 2015.

Camacho, A. G., Fernández, J. and Gottsmann, J.: The 3-D gravity inversion package GROWTH2.0 and its application to Tenerife Island, Spain, Comput. Geosci., 37(4), 621–633, doi:10.1016/j.cageo.2010.12.003, 2011.

Van Camp, M. and Vauterin, P.: Tsoft: graphical and interactive software for the analysis of time series and Earth tides, Comput. Geosci., 31(5), 631–640, doi:10.1016/j.cageo.2004.11.015, 2005.

440   Van Camp, M., Williams, S. D. P. and Francis, O.: Uncertainty of absolute gravity measurements, J. Geophys. Res., 110(B5), B05406, doi:10.1029/2004JB003497, 2005.

Van Camp, M., de Viron, O., Scherneck, H.-G. G., Hinzen, K.-G. G., Williams, S. D. P., Lecocq, T., Quinif, Y. and Camelbeeck, T.: Repeated absolute gravity measurements for monitoring slow intraplate vertical deformation in western Europe, J. Geophys. Res., 116(B8), B08402, doi:10.1029/2010JB008174, 2011.

445   Van Camp, M., de Viron, O., Watlet, A., Meurers, B., Francis, O. and Caudron, C.: Geophysics From Terrestrial Time-Variable Gravity Measurements, Rev. Geophys., 55(4), 938–992, doi:10.1002/2017RG000566, 2017.

Carbone, D. and Greco, F.: Review of Microgravity Observations at Mt. Etna: A Powerful Tool to Monitor and Study Active Volcanoes, Pure Appl. Geophys., 164(4), 769–790, doi:10.1007/s00024-007-0194-7, 2007.

Chang, K.-J., Chan, Y.-C., Chen, R.-F. and Hsieh, Y.-C.: Geomorphological evolution of landslides near an active normal 450 fault in northern Taiwan, as revealed by lidar and unmanned aircraft system data, Nat. Hazards Earth Syst. Sci., 18(3), 709–727, doi:10.5194/nhess-18-709-2018, 2018.

Chen, C. S. and Chen, Y. L.: The rainfall characteristics of Taiwan, Mon. Weather Rev., 131(7), 1323–1341, 2003.

Chiang, S. H. and Chang, K. T.: The potential impact of climate change on typhoon-triggered landslides in Taiwan, 2010-2099, Geomorphology, 133(3–4), 143–151, doi:10.1016/j.geomorph.2010.12.028, 2011.

455   Cook, K. L., Turowski, J. M. and Hovius, N.: A demonstration of the importance of bedload transport for fluvial bedrock erosion and knickpoint propagation, Earth Surf. Process. Landforms, 38(7), 683–695, doi:10.1002/esp.3313, 2013.

Croissant, T., Lague, D., Steer, P. and Davy, P.: Rapid post-seismic landslide evacuation boosted by dynamic river width, Nat. Geosci., 10, 680, 2017.

Crossley, D., Hinderer, J. and Riccardi, U.: The measurement of surface gravity., Rep. Prog. Phys., 76(4), 046101, 460 doi:10.1088/0034-4885/76/4/046101, 2013.

Dadson, S., Hovius, N., Pegg, S., Dade, W. B., Horng, M. J. and Chen, H.: Hyperpycnal river flows from an active mountain belt, J. Geophys. Res. Earth Surf., 110(F4), n/a-n/a, doi:10.1029/2004JF000244, 2005.

Dadson, S. J., Hovius, N., Chen, H., Dade, W. B., Hsieh, M.-L., Willett, S. D., Hu, J.-C., Horng, M.-J., Chen, M.-C., Stark, C. P., Lague, D. and Lin, J.-C.: Links between erosion, runoff variability and seismicity in the Taiwan orogen, Nature, 426, 465   648 [online] Available from: http://dx.doi.org/10.1038/nature02150, 2003.

Darby, S. E., Hackney, C. R., Leyland, J., Kummu, M., Lauri, H., Parsons, D. R., Best, J. L., Nicholas, A. P. and Aalto, R.: Fluvial sediment supply to a mega-delta reduced by shifting tropical-cyclone activity, Nature, 539(7628), 276–279, doi:10.1038/nature19809, 2016.

Deffontaines, B., Chang, K.-J., Champenois, J., Fruneau, B., Pathier, E., Hu, J.-C., Lu, S.-T. and Liu, Y.-C.: Active
470   interseismic shallow deformation of the Pingting terraces (Longitudinal Valley – Eastern Taiwan) from UAV high-resolution topographic data combined with InSAR time series, Geomatics, Nat. Hazards Risk, 8(1), 120–136, doi:10.1080/19475705.2016.1181678, 2017.

Deffontaines, B., Chang, K.-J., Champenois, J., Lin, K.-C., Lee, C.-T., Chen, R.-F., Hu, J.-C. and Magalhaes, S.: Active tectonics of the onshore Hengchun Fault using UAS DSM combined with ALOS PS-InSAR time series (Southern Taiwan),
475   Nat. Hazards Earth Syst. Sci., 18(3), 829–845, doi:10.5194/nhess-18-829-2018, 2018.

Dehant, V., Defraigne, P. and Wahr, J. M.: Tides for a convective Earth, J. Geophys. Res., 104, 1035–1058, 1999.

DeLisle, C. and Yanites, B. J.: The impacts of landslides triggered by the 2009 Typhoon Morakot on landscape evolution: A mass balance approach, in American Geophysical Union, Fall Meeting 2018, abstract #EP21C-2257, vol. 2018, pp. EP21C-2257. [online] Available from: https://ui.adsabs.harvard.edu/abs/2018AGUFMEP21C2257D, 2018.

480   Eltner, A., Kaiser, A., Castillo, C., Rock, G., Neugirg, F. and Abellán, A.: Image-based surface reconstruction in geomorphometry – merits, limits and developments, Earth Surf. Dynam., 4(2), 359–389, doi:10.5194/esurf-4-359-2016, 2016.

Farinotti, D., Longuevergne, L., Moholdt, G., Duethmann, D., Mölg, T., Bolch, T., Vorogushyn, S. and Güntner, A.: Substantial glacier mass loss in the Tien Shan over the past 50 years, Nat. Geosci., 8(9), 716–722, doi:10.1038/ngeo2513,
485   2015.

Ferguson, J. F., Klopping, F. J., Chen, T., Seibert, J. E., Hare, J. L. and Brady, J. L.: The 4D microgravity method for waterflood surveillance: Part 3 — 4D absolute microgravity surveys at Prudhoe Bay, Alaska, GEOPHYSICS, 73(6), WA163–WA171, doi:10.1190/1.2992510, 2008.

Fores, B., Champollion, C., Moigne, N. Le and Chery, J.: Impact of ambient temperature on spring-based relative gravimeter
490   measurements, J. Geod., 91(3), 269–277, doi:10.1007/s00190-016-0961-2, 2017.

Fuller, C. W. W., Willett, S. D. D., Hovius, N. and Slingerland, R.: Erosion Rates for Taiwan Mountain Basins: New Determinations from Suspended Sediment Records and a Stochastic Model of Their Temporal Variation, J. Geol., 111(1), 71–87, doi:10.1086/344665, 2003.

Fuller, C. W. W., Willett, S. D. D., Fisher, D. and Lu, C. Y. Y.: A thermomechanical wedge model of Taiwan constrained by
495   fission-track thermochronometry, Tectonophysics, 425(1–4), 1–24, doi:10.1016/j.tecto.2006.05.018, 2006.

Ge, X., Li, T., Zhang, S. and Peng, M.: What causes the extremely heavy rainfall in Taiwan during Typhoon Morakot (2009)?, Atmos. Sci. Lett., 11(1), 46–50, 2010.

Gelaro, R., McCarty, W., Suárez, M. J., Todling, R., Molod, A., Takacs, L., Randles, C. A., Darmenov, A., Bosilovich, M. G., Reichle, R., Wargan, K., Coy, L., Cullather, R., Draper, C., Akella, S., Buchard, V., Conaty, A., da Silva, A. M., Gu, W.,
500   Kim, G.-K., Koster, R., Lucchesi, R., Merkova, D., Nielsen, J. E., Partyka, G., Pawson, S., Putman, W., Rienecker, M., Schubert, S. D., Sienkiewicz, M. and Zhao, B.: The Modern-Era Retrospective Analysis for Research and Applications, Version 2 (MERRA-2), J. Clim., 30(14), 5419–5454, doi:10.1175/JCLI-D-16-0758.1, 2017.

Han, S. C., Shum, C. K., Bevis, M., Ji, C. and Kuo, C.-Y.: Crustal Dilatation Observed by GRACE After the 2004 Sumatra-Andaman Earthquake, Science, 313(5787), 658–663, doi:10.1126/science.1128661, 2006.

505 Hare, J. L., Ferguson, J. F. and Brady, J. L.: The 4D microgravity method for waterflood surveillance: Part IV — Modeling and interpretation of early epoch 4D gravity surveys at Prudhoe Bay, Alaska, GEOPHYSICS, 73(6), WA173–WA180, doi:10.1190/1.2991120, 2008.

Hartshorn, K., Hovius, N., Dade, W. B. and Slingerland, R. L.: Climate-Driven Bedrock Incision in an Active Mountain Belt, Science (80-.)., 297(5589), 2036 LP – 2038, doi:10.1126/science.1075078, 2002.

510 Hinderer, J., Crossley, D. and Warburton, R. J.: Superconducting Gravimetry, edited by G. B. T.-T. on G. (Second E. Schubert, pp. 59–115, Elsevier, Oxford., 2015.

Horowitz, A. J.: An evaluation of sediment rating curves for estimating suspended sediment concentrations for subsequent flux calculations, Hydrol. Process., 17(17), 3387–3409, doi:10.1002/hyp.1299, 2003.

Horton, A. J., Constantine, J. A., Hales, T. C., Goossens, B., Bruford, M. W. and Lazarus, E. D.: Modification of river
515 meandering by tropical deforestation, Geology, 45(6), 511–514, doi:10.1130/G38740.1, 2017.

Hovius, N., Stark, C. P., Tsu, C. H., Chuan, L. J., Hao-tsu, C., Jiun-chuan, L., Chu, H. T. and Lin, J. C.: Supply and removal of sediment in a landslide-dominated mountain belt: Central Range, Taiwan, J. Geol., 108(1), 73–89, 2000.

Hovius, N., Meunier, P., Lin, C.-W. W., Chen, H., Chen, Y.-G. G., Dadson, S., Horng, M.-J. J. and Lines, M.: Prolonged seismically induced erosion and the mass balance of a large earthquake, Earth Planet. Sci. Lett., 304(3), 347–355,
520 doi:10.1016/j.epsl.2011.02.005, 2011.

Hsieh, M.-L. and Capart, H.: Late Holocene episodic river aggradation along the Lao-nong River (southwestern Taiwan): An application to the Tseng-wen Reservoir Transbasin Diversion Project, Eng. Geol., 159, 83–97, doi:https://doi.org/10.1016/j.enggeo.2013.03.019, 2013.

Huang, M. Y.-F. and Montgomery, D. R.: Altered regional sediment transport regime after a large typhoon, southern
525 Taiwan, Geol. , doi:10.1130/G34826.1, 2013.

Hwang, C., Wang, C. G. and Lee, L. H.: Adjustment of relative gravity measurements using weighted and datum-free constraints, Comput. Geosci., 28(9), 1005–1015, 2002.

IES-AS: GPS LAB, 2015.

Jacob, T., Chery, J., Bayer, R., Le Moigne, N., Boy, J.-P., Vernant, P. and Boudin, F.: Time-lapse surface to depth gravity
530 measurements on a karst system reveal the dominant role of the epikarst as a water storage entity, Geophys. J. Int., 177(2), 347–360, doi:10.1111/j.1365-246X.2009.04118.x, 2009.

Jacob, T., Bayer, R., Chery, J. and Le Moigne, N.: Time-lapse microgravity surveys reveal water storage heterogeneity of a karst aquifer, J. Geophys. Res., 115(B6), B06402, doi:10.1029/2009JB006616, 2010.

Kao, R., Hwang, C., Kim, J. W., Ching, K.-E., Masson, F., Hsieh, W.-C., Le Moigne, N. and Cheng, C.-C.: Absolute gravity
535 change in Taiwan: Present result of geodynamic process investigation., Terr. Atmos. Ocean. Sci., 28(6), 855–875, 2017.

Kazama, T., Okubo, S., Sugano, T., Matsumoto, S., Sun, W., Tanaka, Y. and Koyama, E.: Absolute gravity change

associated with magma mass movement in the conduit of Asama Volcano (Central Japan), revealed by physical modeling of hydrological gravity disturbances, J. Geophys. Res., 1263–1287, doi:10.1002/2014JB011563, 2015.

Letellier, T., Lyard, F. and Lefèvre, F.: The new global tidal solution: FES2004, in Proceedings of the Ocean Surface Topography Science Team Meeting, St. Petersburg, Florida, pp. 4–6., 2004.

Lin, C.-W., Chang, W.-S., Liu, S.-H., Tsai, T.-T., Lee, S.-P., Tsang, Y.-C., Shieh, C.-L. and Tseng, C.-M.: Landslides triggered by the 7 August 2009 Typhoon Morakot in southern Taiwan, Eng. Geol., 123(1), 3–12, doi:https://doi.org/10.1016/j.enggeo.2011.06.007, 2011.

Lin, G.-W. and Chen, H.: Recurrence of hyper-concentration flows on the orogenic, subtropical island of Taiwan, J. Hydrol., 502, 139–144, doi:10.1016/J.JHYDROL.2013.08.036, 2013.

Liu, H. and Pike, W. T.: A micromachined angular-acceleration sensor for geophysical applications, Appl. Phys. Lett., 109(17), 173506, doi:10.1063/1.4966547, 2016.

Liu, Y.-C., Hwang, C., Han, J., Kao, R., Wu, C.-R., Shih, H.-C. and Tangdamrongsub, N.: Sediment-Mass Accumulation Rate and Variability in the East China Sea Detected by GRACE, Remote Sens., 8(10), 777, doi:10.3390/rs8090777, 2016.

Longuevergne, L., Boy, J.-P., Florsch, N., Viville, D., Ferhat, G., Ulrich, P., Luck, B. and Hinderer, J.: Local and global hydrological contributions to gravity variations observed in Strasbourg, J. Geodyn., 48(3–5), 189–194, doi:10.1016/j.jog.2009.09.008, 2009.

Longuevergne, L., Wilson, C. R., Scanlon, B. R. and Crétaux, J. F.: GRACE water storage estimates for the middle east and other regions with significant reservoir and lake storage, Hydrol. Earth Syst. Sci., 17(12), 4817–4830, doi:10.5194/hess-17-4817-2013, 2013.

Ménoret, V., Vermeulen, P., Le Moigne, N., Bonvalot, S., Bouyer, P., Landragin, A. and Desruelle, B.: Gravity measurements below $10^{-9}g$ with a transportable absolute quantum gravimeter, Sci. Rep., 8(1), 1–11, doi:10.1038/s41598-018-30608-1, 2018.

Merriam, J. B.: Atmospheric pressure and gravity, Geophys. J. Int., 109(3), 488–500, doi:10.1111/j.1365-246X.1992.tb00112.x, 1992.

Middlemiss, R. P., Samarelli, A., Paul, D. J., Hough, J., Rowan, S. and Hammond, G. D.: The First Measurement of the Earth Tides with a MEMS Gravimeter, Nature, 531, 614–617, doi:10.1038/nature17397, 2016.

Middlemiss, R. P., Bramsiepe, S. G., Douglas, R., Hough, J., Paul, D. J., Rowan, S. and Hammond, G. D.: Field tests of a portable MEMS gravimeter, Sensors (Switzerland), 17(11), 1–12, doi:10.3390/s17112571, 2017.

Milliman, J. D. and Farnsworth, K. L.: River Discharge to the Coastal Ocean: A Global Synthesis., 2011.

Molnar, P., Anderson, R. S. and Anderson, S. P.: Tectonics, fracturing of rock, and erosion, J. Geophys. Res. Earth Surf., 112(3), 1–12, doi:10.1029/2005JF000433, 2007.

Morera, S. B., Condom, T., Crave, A., Steer, P. and Guyot, J. L.: The impact of extreme El Niño events on modern sediment transport along the western Peruvian Andes (1968–2012), Sci. Rep., 7(1), 11947, doi:10.1038/s41598-017-12220-x, 2017.

Mouyen, M., Masson, F., Hwang, C., Cheng, C.-C., Le Moigne, N., Lee, C. W., Kao, R. and Hsieh, W.-C.: Erosion effects

assessed by repeated gravity measurements in southern Taiwan, Geophys. J. Int., 192(1), 113–136, doi:10.1093/gji/ggs019, 2013.

Mouyen, M., Longuevergne, L., Steer, P., Crave, A., Lemoine, J. M., Save, H. and Robin, C.: Assessing modern river sediment discharge to the ocean using satellite gravimetry, Nat. Commun., 9(1), 3384, doi:10.1038/s41467-018-05921-y, 2018.

Nagy, D.: The prism method for terrain corrections using digital computers, Pure Appl. Geophys., 63(1), 31–39, doi:10.1007/BF00875156, 1966.

Naujoks, M., Weise, A., Kroner, C. and Jahr, T.: Detection of small hydrological variations in gravity by repeated observations with relative gravimeters, J. Geod., 82(9), 543–553, doi:10.1007/s00190-007-0202-9, 2008.

Niebauer, T. M.: Gravimetric Methods – Absolute Gravimeter : Instruments Concepts and Implementation, in Treatise on Geophysics, vol. 3, edited by G. Schubert, pp. 37–57, Elsevier., 2015.

Niebauer, T. M., Sasagawa, G. S., Faller, J. E., Hilt, R. and Klopping, F.: A new generation of absolute gravimeters, Metrologia, 32, 159–180, 1995.

Niethammer, U., James, M. R., Rothmund, S., Travelletti, J. and Joswig, M.: UAV-based remote sensing of the Super-Sauze landslide: Evaluation and results, Eng. Geol., 128, 2–11, doi:https://doi.org/10.1016/j.enggeo.2011.03.012, 2012.

Pail, R., Bingham, R., Braitenberg, C., Dobslaw, H., Eicker, A., Güntner, A., Horwath, M., Ivins, E., Longuevergne, L., Panet, I. and Wouters, B.: Science and User Needs for Observing Global Mass Transport to Understand Global Change and to Benefit Society, Surv. Geophys., 36(6), 743–772, doi:10.1007/s10712-015-9348-9, 2015.

Peizhen, Z., Molnar, P. and Downs, W. R.: Increased sedimentation rates and grain sizes 2-4 Myr ago due to the influence of climate change on erosion rates, Nature, 410(April), 891–897, doi:10.1038/35073504, 2001.

Petrov, L. and Boy, J.-P.: Study of the atmospheric pressure loading signal in very long baseline interferometry observations, J. Geophys. Res., 109(B3), B03405, doi:10.1029/2003JB002500, 2004.

Pfeffer, J., Champollion, C., Favreau, G., Cappelaere, B., Hinderer, J., Boucher, M., Nazoumou, Y., Oï, M., Mouyen, M., Henri, C., Le Moigne, N., Deroussi, S., Demarty, J., Boulain, N., Benarrosh, N. and Robert, O.: Evaluating surface and subsurface water storage variations at small time and space scales from relative gravity measurements in semiarid Niger, Water Resour. Res., 49(6), doi:10.1002/wrcr.20235, 2013.

Rebischung, P., Griffiths, J., Ray, J., Schmid, R., Collilieux, X. and Garayt, B.: IGS08: The IGS realization of ITRF2008, GPS Solut., 16(4), 483–494, doi:10.1007/s10291-011-0248-2, 2012.

Rodell, M., Houser, P. R., Jambor, U., Gottschalck, J., Mitchell, K., Meng, C.-J. J., Arsenault, K., Cosgrove, B., Radakovich, J., Bosilovich, M., Entin*, J. K., Walker, J. P., Lohmann, D., Toll, D., Entin, J. K., Walker, J. P., Lohmann, D. and Toll, D.: The Global Land Data Assimilation System, Bull. Am. Meteorol. Soc., 85(3), 381–394, doi:10.1175/BAMS-85-3-381, 2004.

Schwab, M., Rieke-Zapp, D., Schneider, H., Liniger, M. and Schlunegger, F.: Landsliding and sediment flux in the Central Swiss Alps: A photogrammetric study of the Schimbrig landslide, Entlebuch, Geomorphology, 97(3), 392–406, doi:https://doi.org/10.1016/j.geomorph.2007.08.019, 2008.

605 Scintrex Ltd.: CG-5 Scintrex Autograv System, Operation Manual, Scintrex Limited, Concord, Ontario, Canada, http://www.scintrexltd.com/., 2010.

Steer, P., Huismans, R. S., Valla, P. G., Gac, S. and Herman, F.: Bimodal plio-quaternary glacial erosion of fjords and low-relief surfaces in Scandinavia, Nat. Geosci., 5(9), 635–639, doi:10.1038/ngeo1549, 2012.

Steer, P., Simoes, M., Cattin, R. and Shyu, J. B. H.: Erosion influences the seismicity of active thrust faults., Nat. Commun.,
610 5, 5564, doi:10.1038/ncomms6564, 2014.

Tapley, B. D., Bettadpur, S., Ries, J. C., Thompson, P. F. and Watkins, M. M.: GRACE measurements of mass variability in the Earth system, Science, 305(5683), 503–5, doi:10.1126/science.1099192, 2004.

Torres, A., Brandt, J., Lear, K. and Liu, J.: A looming tragedy of the sand commons, Science, 357(6355), 970–971, doi:10.1126/science.aao0503, 2017.

615 Tu, J. T., Chou, C. and Chu, P. S.: The abrupt shift of typhoon activity in the vicinity of Taiwan and its association with western North Pacific-East Asian climate change, J. Clim., 22(13), 3617–3628, doi:10.1175/2009JCLI2411.1, 2009.

Walling, D. E. and Fang, D.: Recent trends in the suspended sediment loads of the world's rivers, Glob. Planet. Change, 39(1), 111–126, doi:https://doi.org/10.1016/S0921-8181(03)00020-1, 2003.

Water Resources Agency: Hydrological yearbook of Taiwan, 2002.

620 Willett, S. D.: Orogeny and orography: The effects of erosion on the structure of mountain belts, J. Geophys. Res., 104(B12), 28,957-28,981, doi:10.1029/1999JB900248, 1999.

Appendix A: Gravimetric effect of the dolosse

625 Fig. A1a is a picture of the dolosse stacked near the gravity site BA02. Their side L and height H are reported with blue lines for comparison with Figs. A1c-d. They are made of 3 identical patterns, which repeats around the center of the dolosse, and close it. The center of the dolosse and part of his sides are empty. However, due to its limited spatial resolution, the photogrammetry "sees" the dolosse as plain hexagons (Fig. A1b). Our aim is thus to define the ratio k between an actual dolosse and a plain dolosse. This ratio is then multiplied by the average density ρ_c of concrete (2.3×10^3 kg m^{-3}), which the

630 dolosse are made of. This way we obtain an effective dolosse density that we pair to the volume obtained from the photogrammetry and eventually compute the gravitational effect of the dolosse at our study sites.

The volume Vp of a regular hexagon with side L and height H is

$$V = \frac{3}{2}\sqrt{3}\,L^2 H = 4.9 \text{ m}^3 \tag{A1}$$

The volume Vd of the actual dolosse is estimated to 1.6 m^3, using the geometry detailed in Figs. A1c-d.

635 Therefore, we find that the true volume of the dolosse is $k = 1.6/4.9 \cong 0.33$, that is one third of the plain volume, hence its effective density is $2.3k = 0.76 \times 10^3$ kg m^{-3}. The geometry and density of the dolosse were used to compute their gravitational attraction at BA04 and BA05 using a 3-dimensionnal (3D) gravity modelling by prisms methods (Nagy, 1966). This effect is about -15 μGal.

640 **Appendix B: In situ determination of the river materials density**
The in situ densities were determined in three steps

1. Dig a small hole in the material (30-40 cm depth). The excavated material is put in a bucket.

2. The volume of the hole is evaluated by photogrammetry (Fig. B1).

3. Weight the bucket and divide it by the volume to get a density.

645

Tables

Effect	Method	Order of magnitude [μGal]	Uncertainty [μGal]
Solid earth tides	WDD	100	0.1
Ocean tide loading	FES 2004 model	10	0.1
Polar motions	IERS data	1	0.1
Air pressure	Barometer data	0.5-1	0.1
Vertical ground motions	GNSS data	-2-4	1-2
Hydrology	GLDAS2/MERRA2 model	2	5
Dolosse at BA03, BA04	Photogrammetry	-15	5

Table 1: Summary of the corrections applied to our gravity measurements, with their order of magnitude. The uncertainties on the first four corrections are those proposed by Van Camp et al., 2005.

650

Case	Densities (10^3 kg m^{-3})		RMS (μGal)
	River	**Landslide**	
1	$\rho = 1.9 \pm 0.2$ (no distinction river/landslide)		9.6
2	$\rho_r = 1.9 \pm 0.2$	$\rho_l = 2.0 \pm 0.6$	9.5
3	$\rho_r^{1615} = 1.6 \pm 0.6$; $\rho_r^{1716} = 2.0 \pm 0.2$	$\rho_l = 1.7 \pm 0.8$	9.6

Table 2: Densities obtained for each inversion case, with their standard deviation and the root mean square of the residuals *V*.

Figures
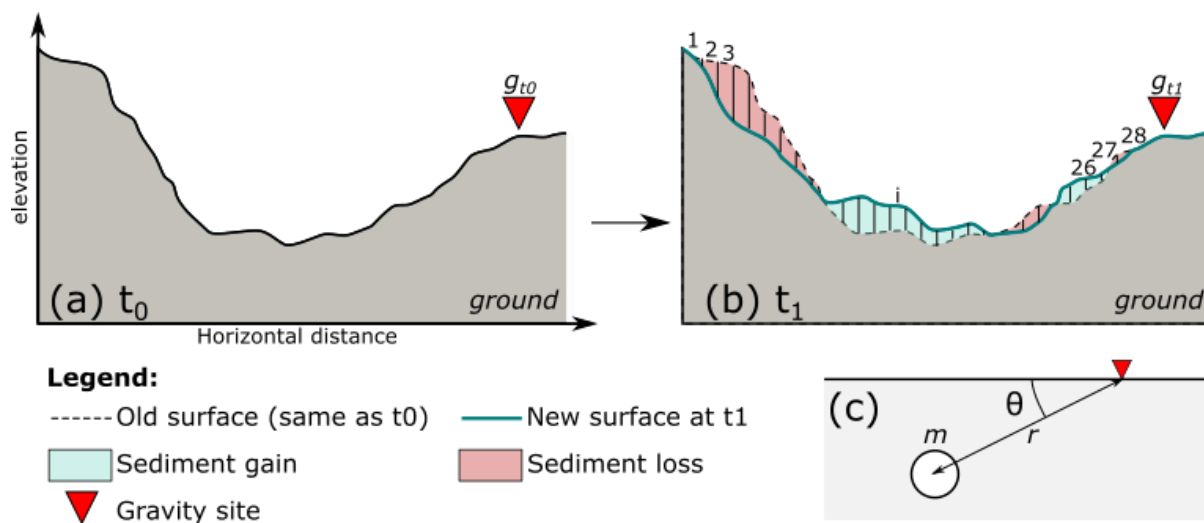
655

Figure 1: a) Ground surface elevation at time t_0, gravity is measured and equal to g_{t0}. **b)** New ground surface at $t_1 > t_0$, after sediment redistributions occurred. The gravity is measured again at the same place and is equal to g_{t1}. **c)** Parameters used for computing a point-mass gravity effect (equation 1, point-mass means that the element is approximated to a point which mass is that of the element).

660

Earth **Surface**
Dynamics
Discussions
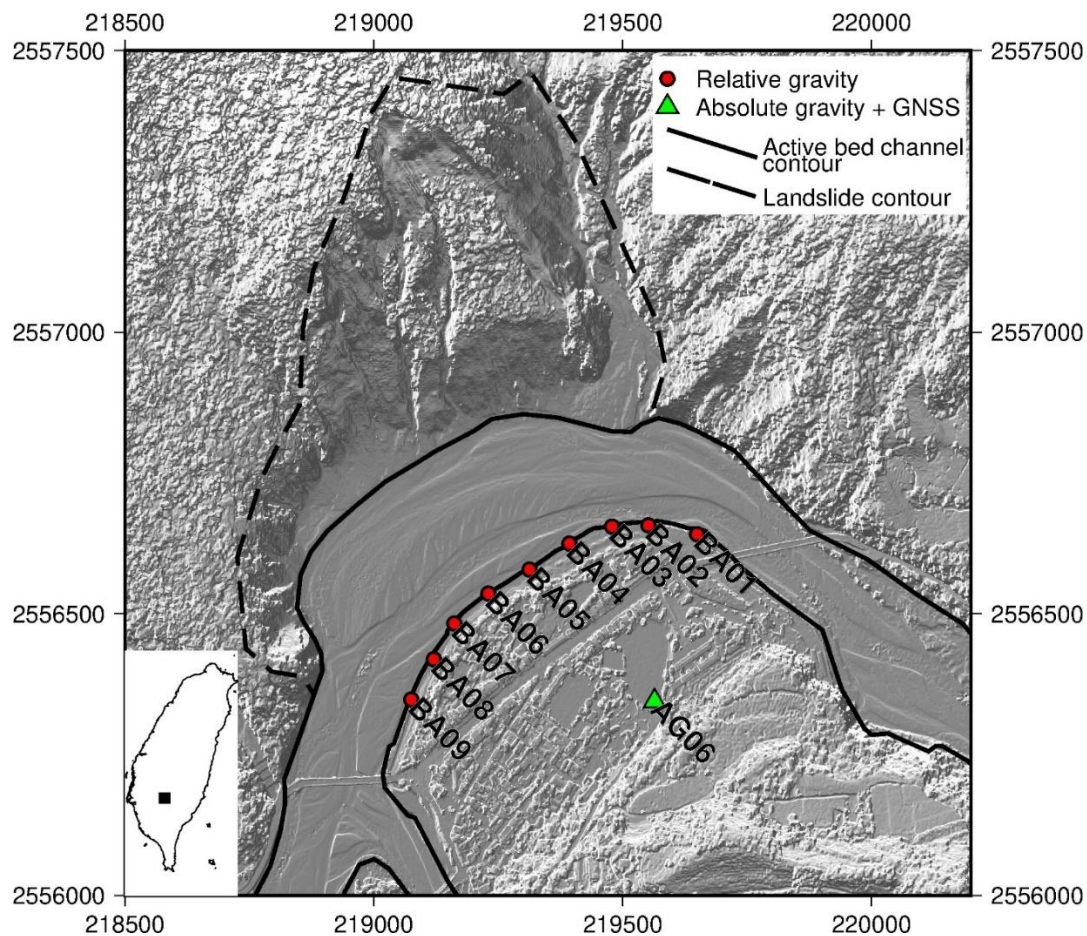
Figure 2: Map of the study area. Absolute gravity measurements are performed only at AG06 while relative gravity measurements are performed at every site. The background image is the hillshaded topography at half-meter resolution obtained by 665 **photogrammetry using an unmanned aerial vehicle (UAV). Inset in the left panel shows the study area in Taiwan. Axis are in meters.**
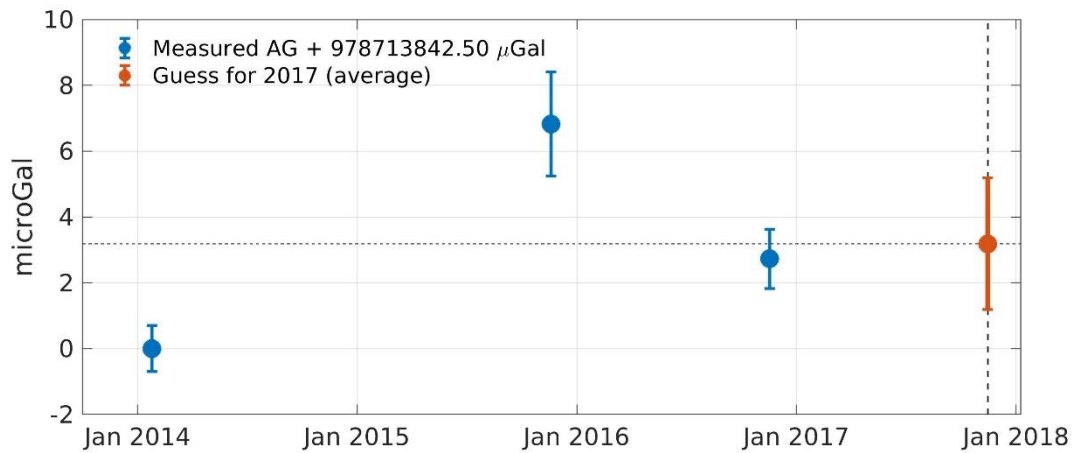
Figure 3: Absolute gravity values measured at AG06 in 2014, 2015 and 2016. In 2017, the absolute gravimeter suffered from a laser problem and no measurement could be done. We thus consider that the value in 2017 is the average of the 2014, 2015 and 2016 values. These absolute gravity values are already corrected for tides, air pressure and polar motions, but not for hydrology and vertical ground displacements yet.

Earth **Surface**
Dynamics
Discussions

EGU

675
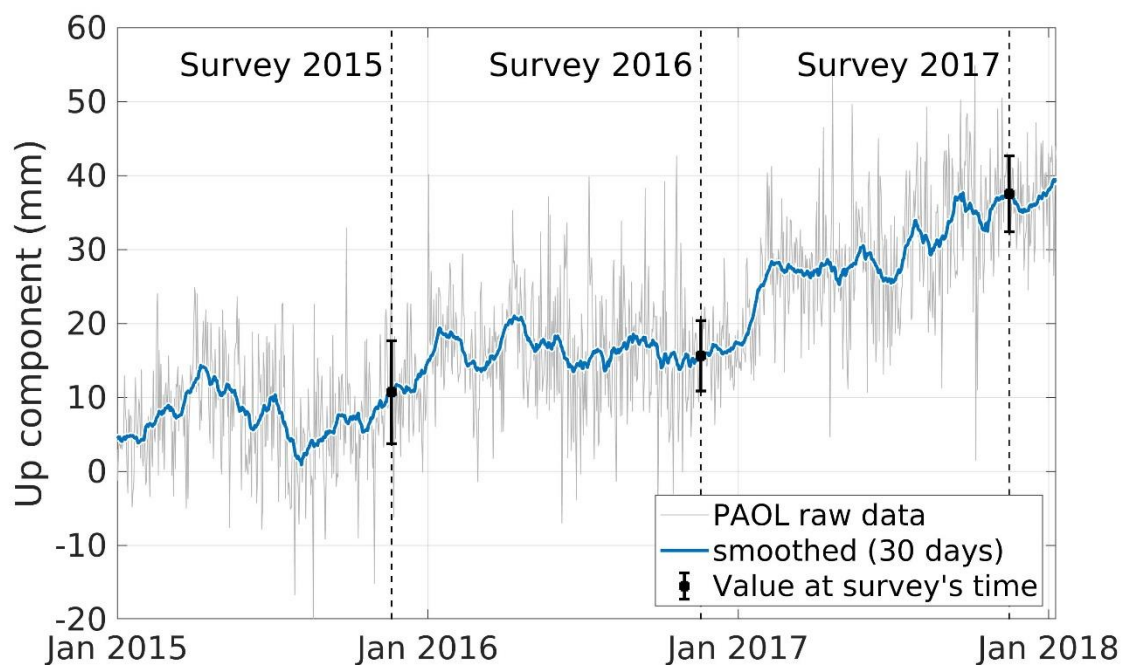
Figure 4: Ground vertical displacements time series at PAOL GPS station, collocated with AG06, provided by the GPSLAB database (IES-AS, 2015). Solutions are computed in the IGS08 reference frame (Rebischung et al., 2012). The time of each joined gravity and photogrammetry survey is shown by dotted lines. The error bar is computed from the standard deviation of the measurements of the same 30-days window.

680
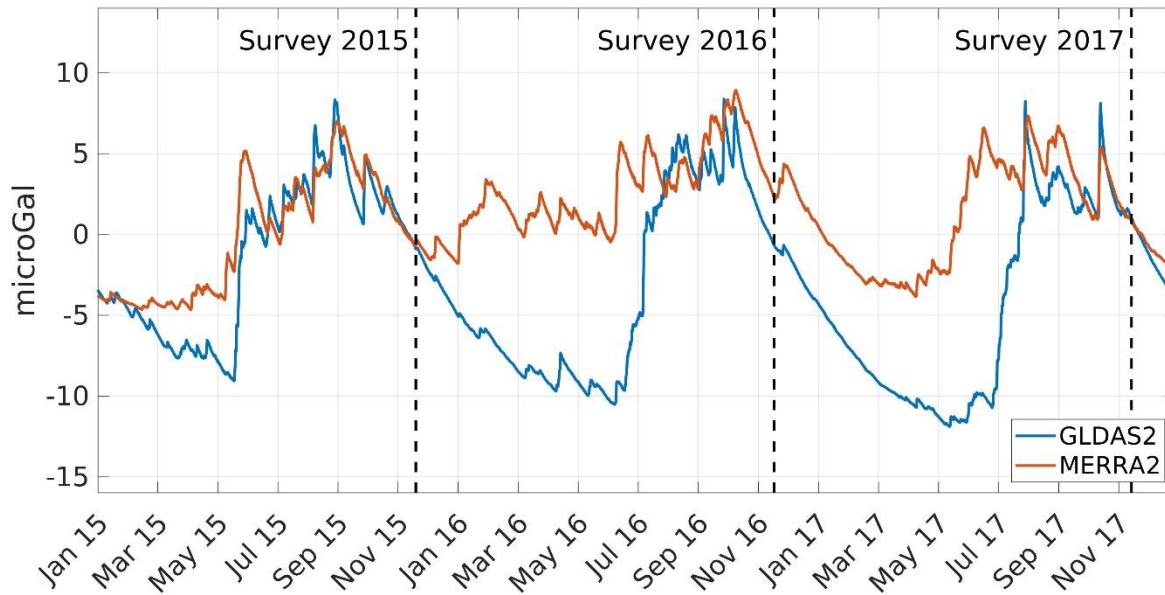
Figure 5: Hydrological effect on gravity at AG06, estimated from global hydrological models GLDAS2 and MERRA2.

685

Earth **Surface**
Dynamics
Discussions
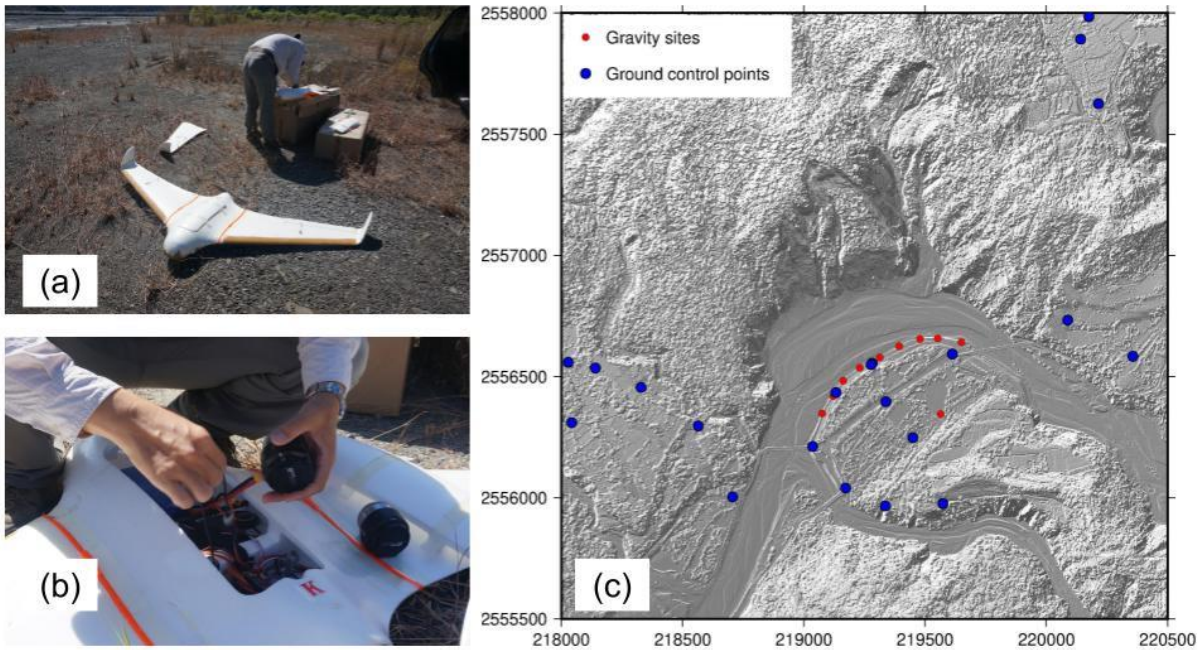
Figure 6: a) UAV, modified Skywalker X8. b) Close-up on the central compartment of the UAV, where the camera and lens are mounted. c) Map of the ground control points with the shaded topography in the background. The gravity sites are also shown for reference.

Earth **Surface**
Dynamics
Discussions
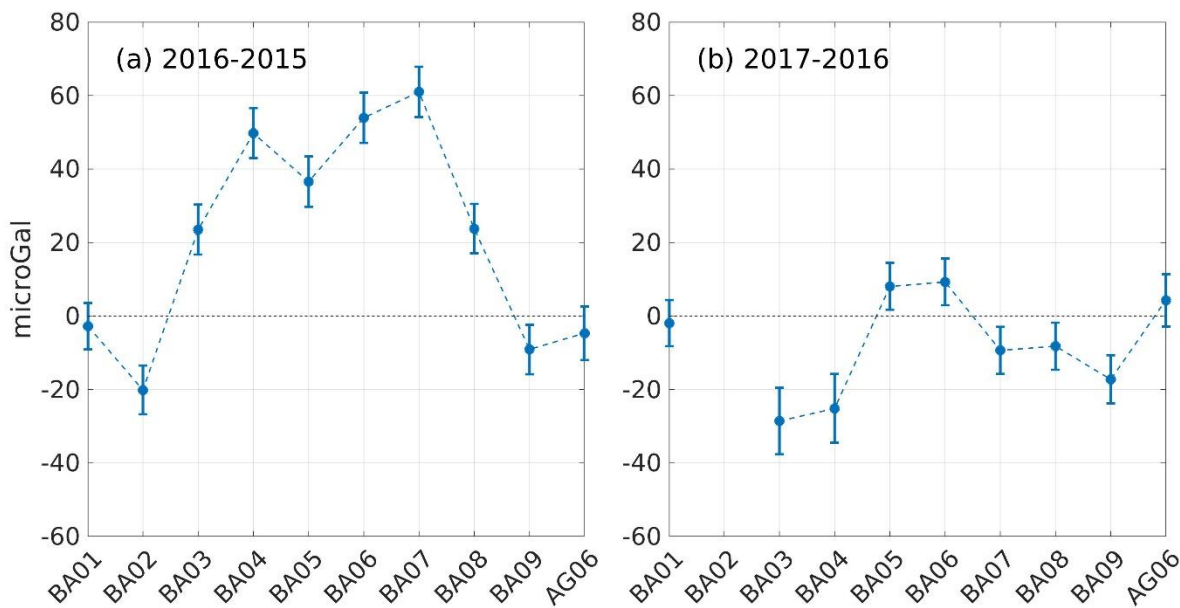
695

Figure 7: Gravity changes between (a) 2015 and 2016 and (b) between 2016 and 2017. BA02 could not be measured in 2017 because of construction work ongoing near the site. The error bars represent $\sqrt{\sum_i \sigma_i^2}$ where σ's are the uncertainties of the gravity measurements and of the seven corrections given in Table 1 (thus i ranges from 1 to 8).

Earth **Surface**
Dynamics
Discussions

700
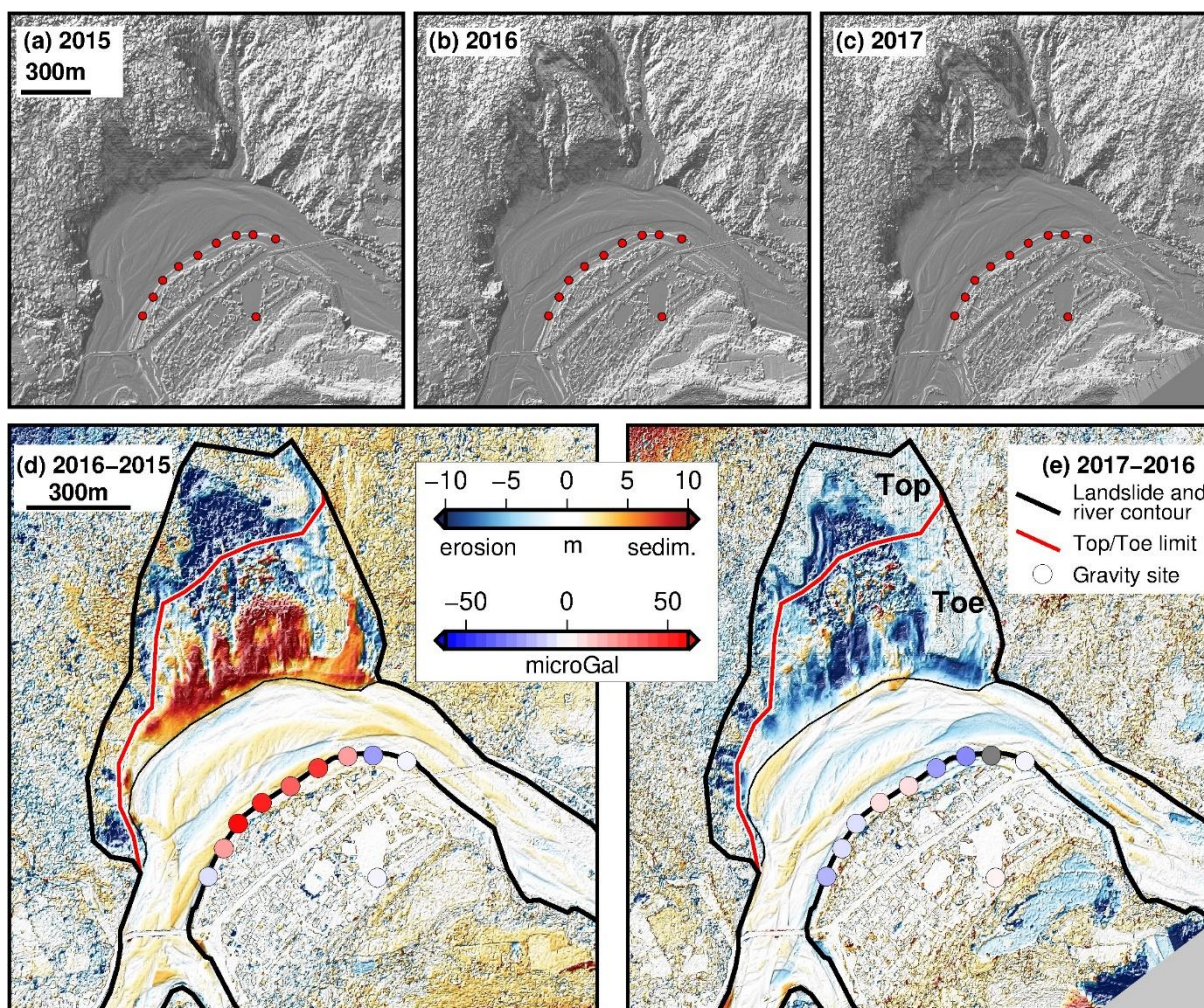
Figure 8: The digital surface models in a) 2015, b) 2016 and c) 2017 and their differences d) between 2016 and 2015 and e) between 2017 and 2016. The disks that locate the gravity sites are colored relative to the gravity change. The black contour line limits the river and the landsliding area. The landsliding area is divided into two parts: the top and the toe. The color scale of the elevation
705 **changes is bounded within ±10 m, which contains 92% of the elevation changes between 2015 and 2016, and 96% of the elevation changes between 2016 and 2017. The extrema are -46 m/33 m between 2015 and 2016, and -38 m/33 m between 2016 and 2017.**

Figure 9: In situ density measured during the 2017 survey (colored dots, the value is also reported in white). Gravity sites are shown with white dots. Axes are in meters. The background is the shaded topography measured during the 2017 survey.

Earth **Surface**
Dynamics
Discussions
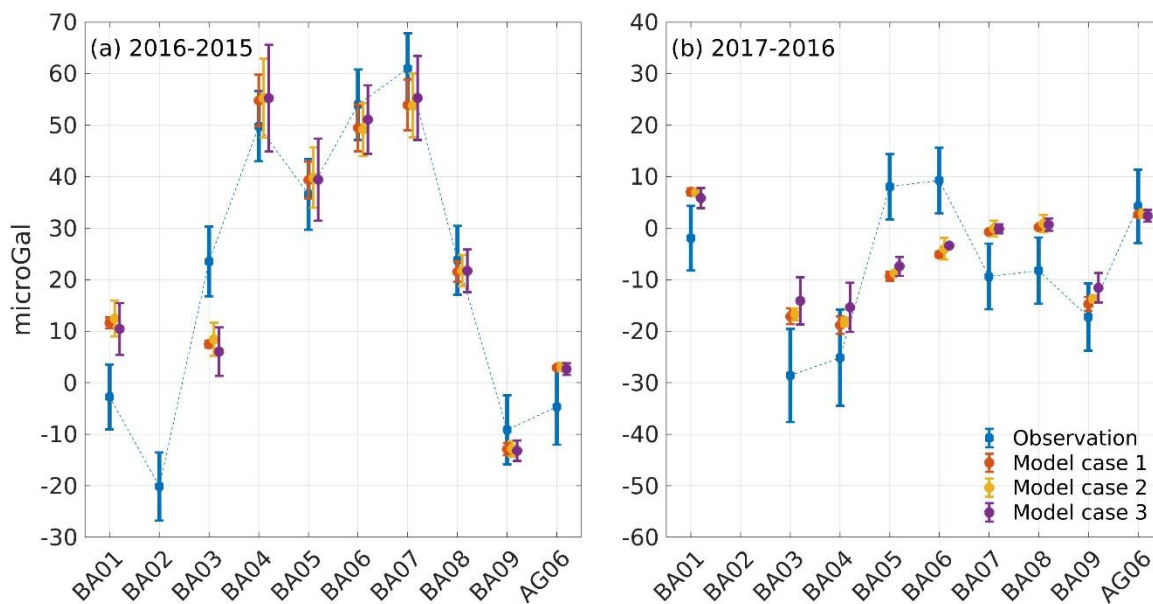
715 **Figure 10: Comparison of the observed (blue) and modelled gravity changes for the densities inverted in cases 1, 2 and 3 (red, yellow and purple, respectively). Each case is slightly offset horizontally for legibility. No gravity is estimated at BA02 since its location is unknown.**

Earth **Surface**
Dynamics
Discussions

EGU

720
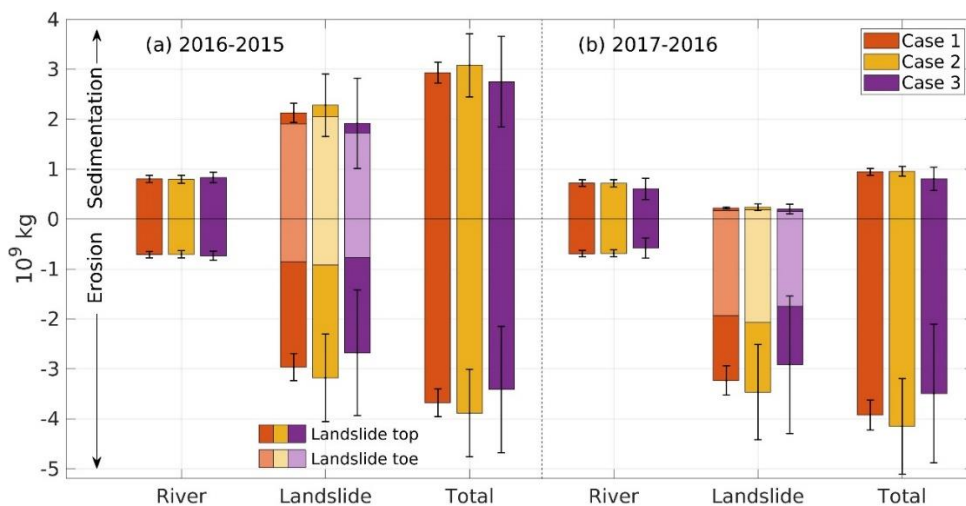
Figure 11: Estimation of the mass of sediment redistributed between 2016 and 2015, and between 2017 and 2016 in cases 1, 2 and 3 (red, yellow and purple, respectively; same color code as in Fig. 10). The mass estimation is shown for the river, the landslide and their sum (total). The error bars are computed by multiplying the volumes variations from the DSM with the densities uncertainties (Table 2). The landslide volumes distinguish the top and the toe of the landslides with a stacked bar plot form.

725

1.
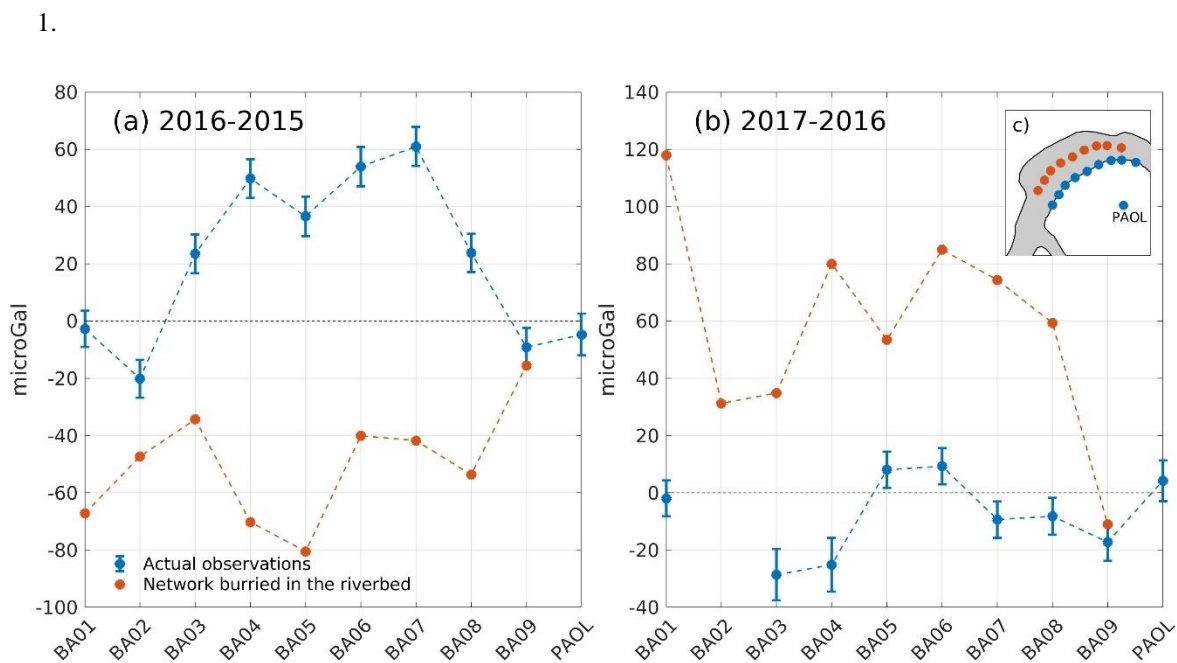
Figure 12: Gravity changes expected at new sites located 5 m beneath the river (red), compared with those measured at BA01-BA09 (blue), for the same sediment redistributions as a) between 2015 and 2016 and b) between 2016 and 2017. The new sites are in fact BA01 – BA09 translated 140 m in the north-east direction, as illustrated in c).

735
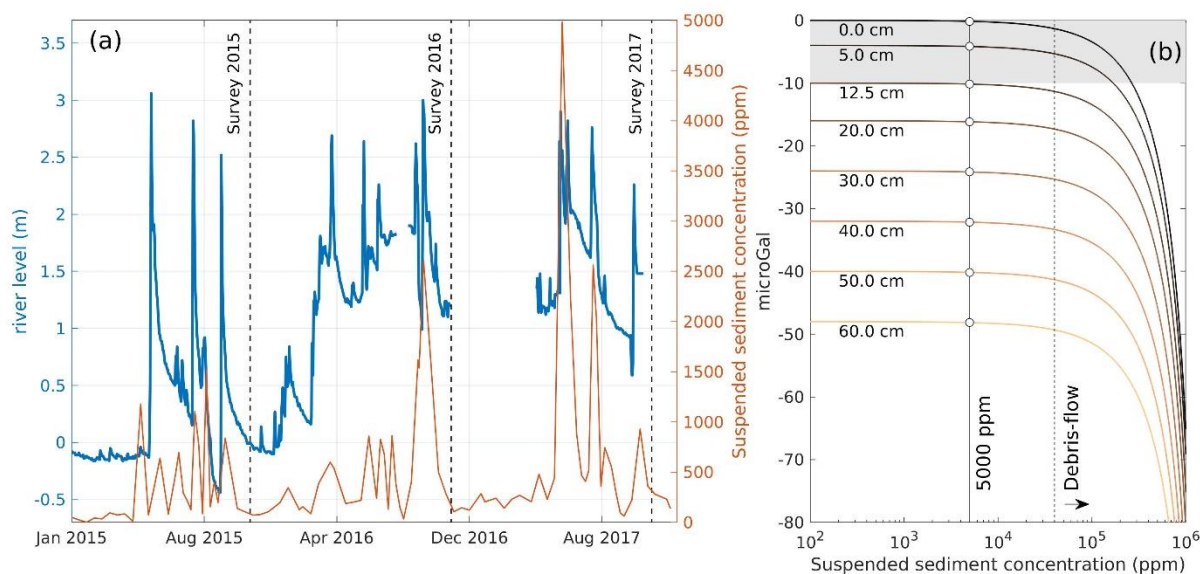
Figure 13: a) River level and sediment concentration of Laonong River, measured at LiuGui station, about 20 km downstream from Paolai. The highest sediment concentration (5000 ppm) is reached in summer 2017, when the river level increased by about 1.6 m. Data are freely available at the Taiwan WRA (Water Resources Agency, 2002). b) Estimated gravity changes at the buried network (Fig. 12c) as a function of the suspended sediment load and of increasing amounts of bedload-transported sediment. The bedload fraction is considered here as a homogenous layer of 0 to 60 cm thickness (labelled on each curve) and density 2×10^3 kg m^{-3}. The river becomes a debris-flow when its suspended sediment concentration goes beyond 4×10^4 ppm. The 5000 ppm level is shown as a reference. Note that the gravity sign is negative because the mass is increased above the gravimeters.

740

745
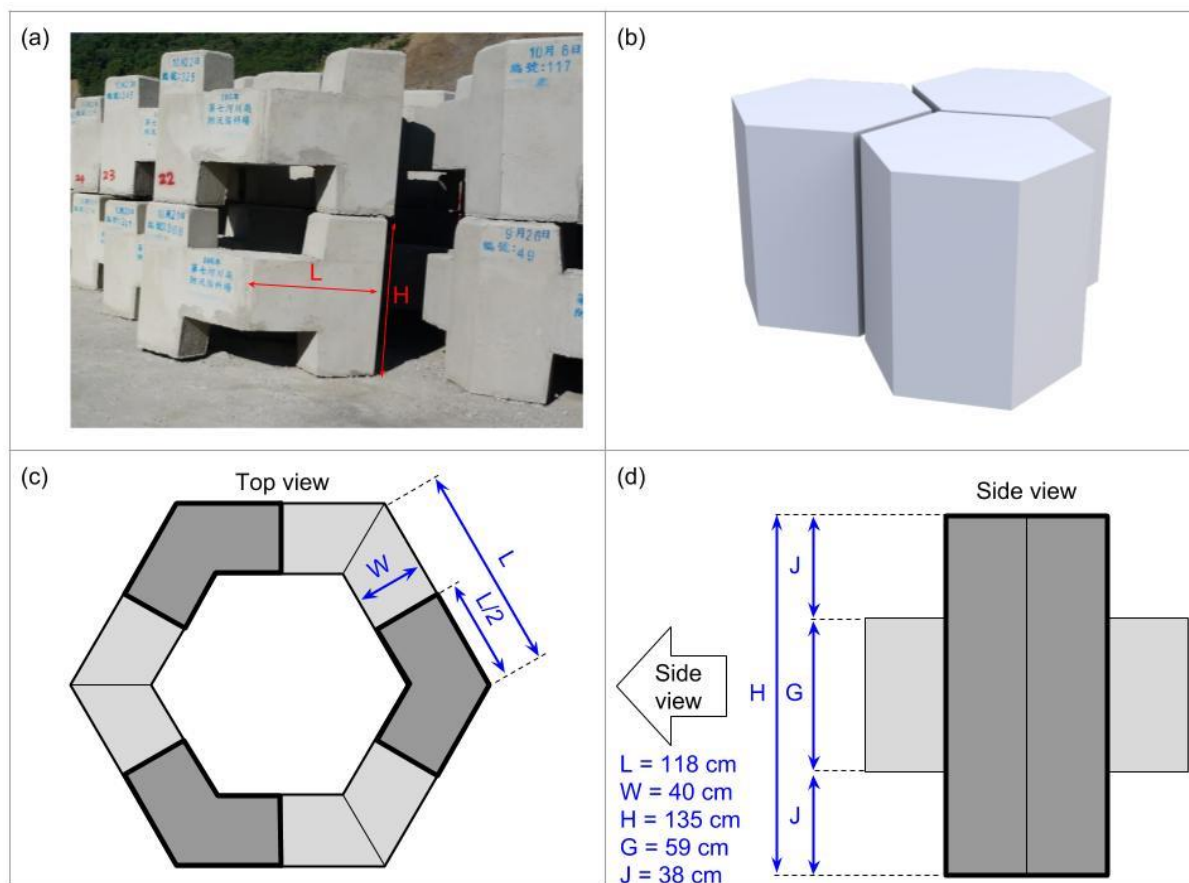
Figure A1: a) Photography of the dolosse. b) 3D hexagonal shape of the plain dolosse, as seen by the photogrammetry. c) Top view of the actual dolosse. The dark gray parts are the pillars actually touching the ground and the light gray parts are the "arms" of the dolosse. d) Side view of one dolosse element. One dolosse consists in three of these parts, 750 joined by the arms.
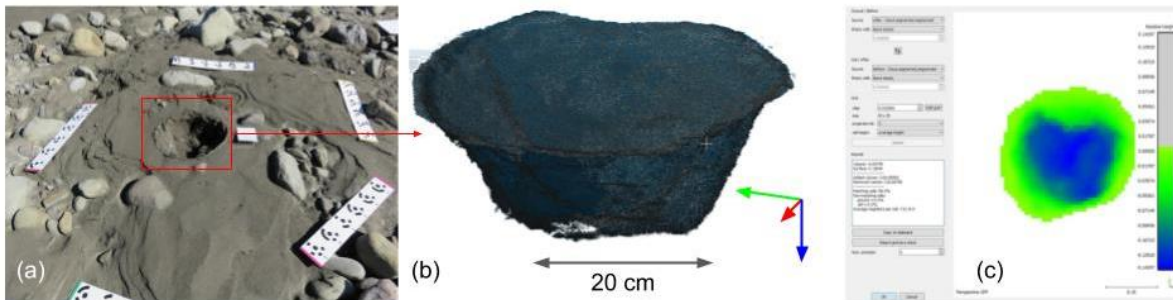
755 **Figure B1: a) Picture of the hole taken with references scales and benchmarks. Several pictures were thus taken before and after the hole was dug. b) 3D cloud of the points mapping the hole surface. c) Computation of the volume bounded by the hole and the former surface of the ground, before the hole was done.**